

Topology Optimization for additive manufacturing with distortion constraints

Misiun, Grzegorz; van de Ven, Emiel; Langelaar, Matthijs; Geijselaers, Hubert; van Keulen, Fred; van den Boogaard, Ton; Ayas, Can

DOI

[10.1016/j.cma.2021.114095](https://doi.org/10.1016/j.cma.2021.114095)

Publication date

2021

Document Version

Final published version

Published in

Computer Methods in Applied Mechanics and Engineering

Citation (APA)

Misiun, G., van de Ven, E., Langelaar, M., Geijselaers, H., van Keulen, F., van den Boogaard, T., & Ayas, C. (2021). Topology Optimization for additive manufacturing with distortion constraints. *Computer Methods in Applied Mechanics and Engineering*, 386, Article 114095. <https://doi.org/10.1016/j.cma.2021.114095>

Important note

To cite this publication, please use the final published version (if applicable).
Please check the document version above.

Copyright

Other than for strictly personal use, it is not permitted to download, forward or distribute the text or part of it, without the consent of the author(s) and/or copyright holder(s), unless the work is under an open content license such as Creative Commons.

Takedown policy

Please contact us and provide details if you believe this document breaches copyrights.
We will remove access to the work immediately and investigate your claim.

Topology Optimization for additive manufacturing with distortion constraints

Grzegorz Misiun^{a,*}, Emiel van de Ven^b, Matthijs Langelaar^b, Hubert Geijselaers^a,
Fred van Keulen^b, Ton van den Boogaard^a, Can Ayas^b

^a University of Twente, Department of Mechanical Engineering, Drienerlolaan 5, 7522NB, Enschede, The Netherlands

^b Delft University of Technology, Department of Precision and Microsystem Engineering, Mekelweg 5, 2628CD, Delft, The Netherlands

Received 13 December 2020; received in revised form 2 August 2021; accepted 2 August 2021

Available online xxx

Abstract

An important cause of failure in powder bed additive manufacturing is the distortion of the part due to thermal shrinkage during printing and the relaxation of residual stresses after its release from the base plate. In this paper, Additive Manufacturing simulations are coupled with Topology Optimization in order to generate designs that are not susceptible to failure associated with distortion. Two possible causes of failure are accounted for: recoater collision and global distortion of the product. Both are considered by simulation of the build process and defined as constraints in the context of a Solid Isotropic Material with Penalization method based topological optimization. The adjoint method is used to derive the sensitivities of the additive manufacturing constraints. The method is demonstrated with the 2D and 3D optimization of a bracket. Next to global topological changes, the obtained designs show features that are aimed at facilitating the printing process. These features resemble supports that are routinely applied to powder bed additive manufacturing. The formulated constraints were found to prevent excessive part distortion and associated build failures in all cases, against a modest increase in the compliance of the bracket.

© 2021 The Authors. Published by Elsevier B.V. This is an open access article under the CC BY license (<http://creativecommons.org/licenses/by/4.0/>).

Keywords: Additive manufacturing; Topology Optimization; Inherent strains; Shape distortions; Recoater collision

1. Introduction

Additive manufacturing (AM) of 3D objects comprises deposition of layer-upon-layer of material. Its undeniable advantage, which distinguishes it from conventional production techniques such as milling, forging or casting is its ability to accommodate virtually unlimited freedom of design [1]. Moreover, AM is characterized by a short lead time, low material waste, the possibility to process hard-to-produce materials (e.g., TiAl and NiCrFe alloys) and the fabrication of products that require less machining due to near-net-shape production. For these reasons, AM techniques are gaining popularity also for metals [2]. The focus of this research is on a particular metal AM method, Selective Laser Melting (SLM), which utilizes a laser beam to melt and fuse metal powder [3]. The SLM process takes place in a special chamber under an inert gas atmosphere. At every build cycle a thin layer of metal powder, typically 40–60 μm thick, is spread by a recoater assuring that the deposited powder layer has a constant thickness.

* Corresponding author.

E-mail address: misiungs@gmail.com (G. Misiun).

Next, the powder layer is selectively melted by the laser beam steered by scanning mirrors. The scanning laser beam thus fuses the powder onto the previously deposited substrate to add a thin layer of metal. After the scanning of a layer has completed, the base plate on which the product is built is lowered by a height equal to the layer thickness, and the above mentioned steps are repeated until the required number of layers have been deposited [1,4].

One of the well-known issues associated with metal 3D printing, that we investigate in this paper, is the distortion of the part [5]. During the layer deposition, the metal powder is melted by energy provided by the laser beam. This heat is conducted to the layers below so there is a temperature difference between subsequent layers. While the top layers are going through melting-solidification cycles, layers sufficiently below stay in the solid state. In the end, the temperature gradients lead to non-uniform thermal strains which in turn give rise to unwanted distortions as well as residual stresses since the bonding between layers partially constrains relaxation of thermal strains [6–8]. As a consequence, dimensional accuracy of the part may be compromised, which leads to laborious post-processing or rejection. In extreme cases, the part may fail due to residual stress exceeding the material limit during the build [5]. The issues that are most frequently encountered are shape distortions after the part has been cut loose from the base plate and collision of the recoater with the unfinished part due to excessive distortions during printing [6].

To prevent such failures and to minimize post-processing, distortions during the printing process can be predicted by simulations. Numerical methods for simulation of additive manufacturing originate from welding simulations. This is due to the obvious resemblance between the processes [9,10]. In both, there is the presence of a moving heat source that is usually described by two ellipsoids, as proposed by Goldak [11]. Moreover, as the process unfolds, new material is added which can be considered in a Finite Element (FE) setting by methods for adding elements to the simulation domain. Michaleris [12] compared two of the available element deposition methods: ‘inactive elements’ and ‘quiet elements’. In the inactive element method elements are absent from the calculation until their virtual deposition takes place. The quiet element method, on the other hand, has all the elements active from the outset, but elements representing the part of the domain that has not yet been deposited are assigned an extremely small stiffness and thus the name ‘quiet’. The FE solution for the quiet-element method takes more time, especially at the beginning of the simulation, due to the larger matrix size, which includes also the unnecessary elements. In the inactive elements method, the solver initialization and equation renumbering is performed every time when new elements are introduced, which also affects computational time. To tackle the aforementioned issues, Michaleris proposed a new hybrid approach that combines advantages of both methods and resulted in reduced computational time [12].

In order to predict mechanical field quantities such as distortions and residual stresses, one-way coupled thermo-mechanical simulations are frequently employed while the behavior of the melt pool is neglected. In a one-way coupled thermo-mechanical simulation temperatures obtained from a thermal model are used to generate loads in a mechanical simulation [13–16]. When the behavior of the melt pool is not explicitly modeled, it is imitated by a change in material properties [17–19].

In SLM, compared to welding, the heat source is much smaller relative to the part size. This difference in length scales gives rise to a need for very fine spatial discretization of a large domain, which leads to a high number of degrees of freedom in a FE setting. Therefore, simulations of AM are much more computationally demanding than those of welding and the numerical methods which were developed for welding simulations are insufficient [12,20]. The development of numerical models that are capable of predicting the temperature evolution and the associated distortions in a computationally efficient way has been a topic of ongoing research, of which the main developments are reviewed below.

First attempts to predict the distortions during additive manufacturing used a commercial FE software package. ABAQUS has been used to simulate deposition of several material layers in a simplified 1D-thermal and 2D-mechanical model [21,22]. Matsumoto et al. [23] used their in-house software to simulate deposition of a single layer. Simulations performed in 3D can be found in [24,25], where the hatching of a single layer was simulated using a 3D model based on ABAQUS and ANSYS software packages. For different innovative approaches, the work of Hodge et al. [26] may be counted. Here not only material that is going to be solidified is simulated but also the domain that is filled with powder is considered. As the heat source travels it changes the properties of the heated material from powder to solid. Although this is in line with the real metal 3D printing process and is certainly insightful on a small scale, it still seems impractical for application to part scale simulations due to the enormous mesh size that would be required.

An interesting technique was developed for the 3DSIM package which is now part of ANSYS [27–29]. Within this framework, a method for fast mesh refinement has been proposed that allows for simulation speed-up by having

a detailed mesh that follows the heat source. Moreover, there are other practical techniques, which also gained attention from the industry. For instance, a multiscale approach can be mentioned, where computational demands are reduced by performing simulations with different levels of complexity on different scales. Results from finer scales are used as data in the coarser scale, for example in the form of inherent strains [30–33]. Usually, at the microscale a single laser scanning line is simulated, the mesoscale applies to a hatch, i.e. an area covered by several laser scanning lines, and the macroscale addresses several layers or even a whole part.

Besides aforementioned approaches, two additional modeling techniques are often used: ‘inherent strains’ and ‘layer lumping’. When inherent strains are prescribed, the simulation of the thermal history is fully replaced by its mechanical equivalent of shrinkage. This means that the thermal shrinkage that occurs during cooling down is calculated in advance and is prescribed as mechanical strain, or the associated stress. Usually, this is applied to a whole layer at once. Then complex thermal calculations can be fully neglected on a part scale, based on the information from lower-scale simulations or experiments [14,32,34]. The idea behind layer lumping is to reduce the size of the FE mesh and the number of deposition increments by applying an element size that is bigger than a single layer thickness. Consequently, several layers of material are deposited simultaneously, which substantially reduces the computational burden [32–37].

At this moment many of the aforementioned methods for 3D printing simulations have been implemented and are available as part of commercial FEM packages. Prediction of global distortion in a reasonable time frame has been made possible, although accuracy of the results is questionable, especially for complex shapes [38,39].

Topology optimization (TO) is a mathematical technique which looks for the optimal part layout (material distribution) for a given use case (objective function) under relevant restrictions (constraints). It typically creates complex designs, which cannot be realized with traditional manufacturing techniques [40]. As mentioned before, geometrical complexity is much less a limiting factor in design for AM since it offers a vastly larger freedom compared to traditional manufacturing processes to realize a desired geometry. Therefore, additive manufacturing and topology optimization seem like a perfect match. Some of the results and challenges of application of TO to AM are reviewed in [41].

None of the available commercial simulation software couples TO with numerical modeling of distortion due to 3D printing. The state-of-the-art of dealing with part distortion is based on geometry compensation [31,42]. This is a crude approach since the dependence of distortion is nonlinear with respect to geometrical changes and many iterations may be needed. If distortions can be calculated, it is in principle possible to add them as constraints in an optimization scheme. Our interest is therefore in integrating prediction of distortions in Additive Manufacturing with Topology Optimization. Then it will be possible to obtain designs that are not only optimal for a selected purpose but are also manufacturable through AM without exhibiting failure.

Although the coupling of numerical modeling of AM with TO seems an obvious next step regarding distortion control, to the best of our knowledge only few attempts have been reported so far. In [43] minimization of compliance combined with thermal distortions induced by AM was investigated. For the purpose of thermal modeling two numerical models were used. In the first model, cooling was assigned to all elements at once. This was realized by changing the part temperature from an initial to a final value in one step which causes deformations due to thermal contraction. In the second model, cooling was assigned in the same manner but this time combined with an element birth scheme, where mesh activation was performed incrementally element by element. Results for 2D and 3D problems were presented for different boundary conditions. Although the novelty of this study is undeniable, its application to engineering problems seems infeasible. Due to the calculation of sensitivities through finite differences, time complexity and thus calculation time of the optimization largely increase with the number of design variables. This will make optimization inefficient especially for the element birth model, where for a single printing simulation many incremental steps are to be calculated.

In [13] numerical modeling is combined with topology optimization based on the level-set method. Thermo-elastic numerical models of 3D printing were used with the design domain consisting of two subdomains: powder and solid. The models are transient in time to simulate the cooling down and an adjoint method was used for the calculation of sensitivities. The considered objectives were the minimization of thermal stresses or minimization of the amount of the vertical displacement of just deposited layers exceeding an allowed threshold. The latter is relevant to prevent recoater collisions, where the recoater roller or rake can hit the partially built part due to its distortions. Often such an event marks the breakdown of the printing process. The optimized designs achieve improvements for the considered objective functions.

Takazewa et al. [44] also performed part shape optimization but used lattice structures instead of solid material. The goal was to minimize printing distortions at selected nodes. For optimization purposes, COMSOL Multiphysics software was used, and to prescribe shrinkage loads inherent strains were applied. Inherent strains were calibrated by numerical modeling done in Simufact Additive. The method was verified on 2D and 3D examples, but considered optimization domains were rather small.

Other contributions that incorporate printing simulation are by Bartsch et al. [45], Cheng et al. [46], Pellens et al. [47] and Zhang et al. [48]. These works focus on optimizing the support structures instead of optimizing the part shape. Supports are slender structures that are introduced into the printing job in order to help with the manufacturing process. They reduce local overheating, allow for printing of overhangs and reduce distortions. After the printing, supports are removed and therefore play a role only during the production. By changing their distribution it is possible to influence the printing while preserving the part shape.

Bartsch et al. [45] proposed a method for optimization of supports distribution to maximize stiffness under a given loading condition. First, a printing simulation is performed. The maximal forces calculated during simulation are next used as loads in the topology optimization. Cheng et al. [46], on the other hand, optimized support distribution with the use of graded lattice structures. In this method, a whole design domain is filled with a lattice structure with varying density. The obtained optimization results provide density distributions that reduce residual stresses. The results have been confirmed with experiments. Pellens et al. [47] proposed a method for the limitation of recoater collision by tailoring the support distribution. The optimization's objective was to minimize support volume while setting a constraint on maximal vertical distortions of just deposited elements. As supports, lattice structures were used and to model material shrinkage the inherent strain method was applied. The method was verified on both 2D and 3D examples, considering a beam geometry. Zhang et al. [48] also investigated lattice-based supports for distortions minimization. Optimizations were performed with gravitational load considered and with gravitational loads combined with the inherent strains method. The goal was to minimize distortions under these two loading conditions for different values of allowed volume. The method was verified on a 3D beam geometry and results were confirmed experimentally.

So far there is no approach or tool available which couples Topology Optimization with Additive Manufacturing to find the optimal design of a part while assuring that it is printable and which is also based on a numerical method that can perform 3D printing simulations on a part scale in a reasonable time. Our goal is therefore to focus on a suitable technique for simulation of distortions in full scale 3D printing. The results from these simulations will then serve as constraints in topology optimization of a structural part. The considered AM constraints are distortions of a part measured after the separation from the base plate, and recoater collision. Other constraints, such as overhang criteria, are deliberately omitted given the focus on the effect of distortion control.

In Section 2, the numerical model of AM that is used for the calculation of printing distortion is introduced. In Section 3 the TO model is described, followed by the formulation of constraints that stem from the distortions during the AM process. The derivation of sensitivities of these constraints for application in the numerical optimization is given in an [Appendix](#). Capabilities of the proposed approach are illustrated in Section 4 on 2D and 3D examples.

2. Numerical model of SLM

For simulation of 3D printing, the Finite Element method is used. The simulation is divided into two stages, the printing and the subsequent release stage. A structured finite element mesh is used, with layers of elements arranged perpendicular to the build direction. During the printing stage, step by step, new layers of elements are activated, strains corresponding to thermal shrinkage are prescribed and distortions are calculated. Printing takes place on the base plate. The presence of the base plate is simulated by suppressing displacements of the bottom layer of nodes. When the printing has finished the printed part is released from the base plate. In the release stage, the suppressed degrees of freedom are released and the residual stresses present in the part cause additional distortions.

In the printing simulation, the element birth technique [12] has been adopted, which is combined with the layer lumping technique [37]. To simulate thermal contraction of newly deposited layers an inherent strain technique [14] is used. Finally, geometric linearity is assumed, which means that the displacement vector obtained after every deposition step is not used to update nodal positions.

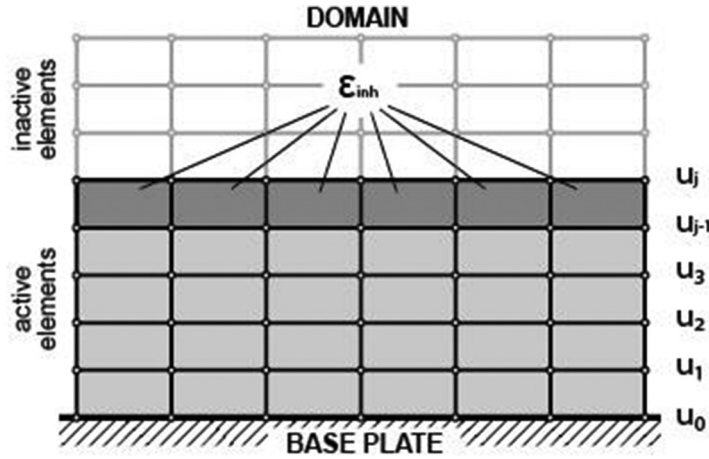


Fig. 1. Schematic illustration of element activation and inherent strain assignment during 3D printing simulation.

2.1. Additive manufacturing simulation by finite element method

The building stage of a workpiece is simulated as the deposition of M lumped layers of elements, followed by an $(M + 1)$ th step to simulate the release from the build plate. In our notation a vector $\mathbf{x}^{(i)}$ refers to a field quantity consists only of the i th building step and a vector \mathbf{x}_j refers to a subset of a field quantity referring only to the j th layer of finite element nodes. Consequently $\mathbf{x}_m^{(n)}$ is a vector referring to the m th layer of nodes when the n th building step is completed. This implies $m \leq n$. Initially, the domain consists only of inactive elements and with every new step one element layer is activated. A schematic illustration of the printing process simulation and the notation is shown in Fig. 1.

Printing always starts from a base plate. The displacement degrees of freedom of nodes connected to the base plate, \mathbf{u}_0 are completely suppressed. After deposition of $j - 1$ element layers, i.e. at the $(j - 1)$ th step, the total set of degrees of freedom is $\mathbf{u}^{(j-1)} = [\mathbf{u}_0^T, \mathbf{u}_1^T, \mathbf{u}_2^T, \dots, \mathbf{u}_{j-1}^T]^T$, where \mathbf{u} are displacement degrees of freedom. Deposition of a new set of material layers starts with activation of a new layer of elements. The degrees of freedom of the newly activated row, \mathbf{u}_j , are added to the current set of degrees of freedom:

$$\mathbf{u}^{(j)} = [\mathbf{u}^{(j-1)T}, \mathbf{u}_j^T]^T = [\mathbf{u}_0^T, \mathbf{u}_1^T, \mathbf{u}_2^T, \dots, \mathbf{u}_{j-1}^T, \mathbf{u}_j^T]^T \tag{1}$$

and a discretized Finite Element equation is set up as:

$$\mathbf{K}^{(j)} \Delta \mathbf{u}^{(j)} = \mathbf{f}^{(j)}, \tag{2}$$

where $\Delta \mathbf{u}^{(j)}$ is the displacement increment calculated for step j where

$$\mathbf{K}^{(j)} = \int_{V^{(j)}} \mathbf{B}^T \mathbf{D} \mathbf{B} dV, \tag{3}$$

and

$$\mathbf{f}^{(j)} = - \int_{V_j} \mathbf{B}^T \mathbf{D} \boldsymbol{\epsilon}_{inh} dV. \tag{4}$$

Here $V^{(j)}$ is the current deposited volume including step j and V_j is the volume of the last (j th) added layer, \mathbf{D} is the isotropic elastic material matrix, the matrix \mathbf{B} is utilized to evaluate strains from nodal displacements and $\boldsymbol{\epsilon}_{inh}$ is the inherent strains vector. Since the model is formulated in terms of incremental displacements, only the inherent strains in the last deposited layer contribute to the right hand side in Eq. (4).

In the inherent strains approach thermal contraction due to the cooling of the material is calculated beforehand and its mechanical equivalent is applied in accordance with

$$\boldsymbol{\epsilon}_{inh} = \alpha \Delta T, \tag{5}$$

where α is the thermal expansion tensor. ΔT is the temperature change during the layer cool down and it determines the negative sign in Eq. (4). Consequently, thermo-mechanical multi-incremental calculations may be replaced by a single mechanical increment. The method itself originates from welding simulations [49]. The value of inherent strains may either be assumed from Eq. (5) [13], calculated from thermo-mechanical simulations performed on a finer scale [50] or obtained experimentally [51], depending on the desired accuracy and available resources.

For the solution of Eq. (2) the suppressed degrees of freedom $\Delta \mathbf{u}_0$ are eliminated from the system of equations. The set of degrees of freedom is partitioned into suppressed ones $\Delta \mathbf{u}_0$ and the ones to be determined $\Delta \mathbf{u}_f^{(j)} = [\Delta \mathbf{u}_1^T, \dots, \Delta \mathbf{u}_j^T]^T$:

$$\begin{bmatrix} \mathbf{K}_{00} & \mathbf{K}_{0f} \\ \mathbf{K}_{f0} & \mathbf{K}_{ff} \end{bmatrix}^{(j)} \begin{Bmatrix} \mathbf{0} \\ \Delta \mathbf{u}_f \end{Bmatrix}^{(j)} = \begin{Bmatrix} \Delta \mathbf{r}_0 \\ \mathbf{f}_f \end{Bmatrix}^{(j)}. \quad (6)$$

In a standard finite element code, usually only $\mathbf{K}_{ff}^{(j)}$ needs to be assembled since the solution for the suppressed degrees of freedom is known to be equal to zero. To calculate distortion upon release from the base plate, it is necessary to track reaction forces \mathbf{r}_0 for which the submatrix \mathbf{K}_{0f} must be used. The reaction forces at the base plate are found as:

$$\mathbf{r}_0^{(j)} = \mathbf{r}_0^{(j-1)} + \mathbf{K}_{0f}^{(j)} \Delta \mathbf{u}_f^{(j)}; \quad j = 1..M, \quad \text{where } \mathbf{r}_0^{(0)} = \mathbf{f}_0^{(1)}. \quad (7)$$

Note that $\Delta \mathbf{u}_f^{(j)}$ has a different size for every step j during the build stage. Inspection of matrix \mathbf{K}_{0f} shows that it only contains non-zero terms connected with degrees of freedom $\Delta \mathbf{u}_1$ of the first layer. In \mathbf{K}_{0f} the number and position of non-zero entries do not change during the build process: \mathbf{K}_{01} . For ease of notation, the form of Eq. (7) is retained, including the step reference (j), because the size of \mathbf{K}_{0f} (number of added zero columns) does change per step. $\mathbf{f}_0^{(1)}$ are forces that act on suppressed degrees of freedom resulting from the inherent strains (see Eq. (4)) in the first deposited layer.

The total displacements of nodes in row i , due to shrinkage of later added layers, until layer j ($j \geq i$) can be calculated as:

$$\mathbf{u}_i^{(j)} = \sum_{k=i}^j \Delta \mathbf{u}_i^{(k)}. \quad (8)$$

For each step, a geometrically linear analysis is performed, which means that the calculated displacements are not used to update nodal positions. Consequently, all layer deposition steps during the building stage can be treated as independent linear problems, which can be solved in parallel [52].

2.2. Distortion after release from the base plate

After the building process has been completed, the workpiece will contain residual stresses which cause the reaction forces $\mathbf{r}_0^{(M)}$ in the suppressed degrees of freedom at the base plate. Release from the base plate is accomplished by releasing the suppressed degrees of freedom and relaxing the residual stresses to a new equilibrium.

Upon release, the workpiece should remain sufficiently supported by a statically determinate set of degrees of freedom to suppress rigid body motion. To this end, for the release step ($M + 1$) all degrees of freedom $\mathbf{u}^{(M)}$ are partitioned into the set of suppressed degrees of freedom $\mathbf{u}_s^{(M+1)}$ and the remainder $\mathbf{u}_f^{(M+1)}$. The distortions upon release are calculated from:

$$\mathbf{K}_{ff}^{(M+1)} \Delta \mathbf{u}_f^{(M+1)} = -\mathbf{r}_f^{(M+1)}, \quad (9)$$

where \mathbf{K}_{ff} is the partition of the stiffness matrix related to the unsuppressed degrees of freedom and $\mathbf{r}_f^{(M+1)}$ are the reaction forces in the released base plate degrees of freedom:

$$\mathbf{r}_f^{(M+1)} = \mathbf{S}_f \mathbf{r}_0^{(M)}, \quad (10)$$

where the matrix \mathbf{S}_f selects the degrees of freedom from those previously clamped to the base plate, which are now released. The result of the selection is a vector of the same length as $\Delta \mathbf{u}_f^{(M+1)}$ with all entries but the ones corresponding to $\mathbf{r}_0^{(M)}$ equal to zero.

The total vector of degrees of freedom $\Delta \mathbf{u}^{(M+1)}$ is identical to that of the last build step $\Delta \mathbf{u}^{(M)}$ since no additional element layer has been activated. The set of free degrees of freedom $\Delta \mathbf{u}_f^{(M+1)}$ pertaining to the release step differs from $\Delta \mathbf{u}_f^{(M)}$ for the last build step. Therefore stiffness matrix partition $\mathbf{K}_{ff}^{(M+1)}$ differs from partition $\mathbf{K}_{ff}^{(M)}$.

Note that for calculation of distortion upon release, reaction forces in the suppressed base plate nodes are monitored instead of the internal stresses. Both approaches are equivalent, but the reaction force vector option has been chosen because it provides a simpler and more intuitive description of the system for the adjoint sensitivities calculations. The obtained solution for the deformation upon release is unique as long as the problem is linear.

3. Topology optimization

In topology optimization, an optimal material distribution within a given design space is calculated to optimize a desired performance [53]. In structural topology optimization, the most common objective to be minimized is compliance, while the allowed material volume is constrained to a specific percentage of the design space.

In this paper, the SIMP (Solid Isotropic Material with Penalization) method is used [40]. The design space is divided into a regular mesh containing N_e identically sized finite elements, each with volume V_0 . The design variables are the element material densities ρ ($0 < \rho_i \leq 1, i = 1, \dots, N_e$) that describe the material distribution. Here $\rho = 0$ indicates void, while $\rho = 1$ represents full presence of material. To promote designs with a preference for ρ either zero or one, so called ‘crisp’ designs, the element contribution to the stiffness matrix is calculated with a penalty exponent p :

$$\mathbf{K}_i = \rho_i^p \int_{V_0} \mathbf{B}^T \mathbf{D} \mathbf{B} dV = \rho_i^p \mathbf{K}_0, \quad i = 1, \dots, N_e. \tag{11}$$

To prevent checkerboard solutions and mesh size dependent solutions regularization by density filtering with a conical weighting function [54] is applied.

Also in this paper, a structure is desired, that minimizes compliance (maximizes stiffness) under a prescribed load with a constraint on maximal allowable structure volume. Additionally, constraints on distortions due to Additive Manufacturing during and after printing will be applied. These constraints will be addressed in Section 3.1. Moreover, bounds on element density will be prescribed and the structure is required to be in equilibrium with the applied loads. The optimization problem is mathematically formulated as:

$$\begin{aligned} \min_{\rho} : \quad & c(\rho) = \mathbf{f}_c^T \mathbf{u}_c, \\ \text{s.t.:} \quad & \frac{1}{N_e} \sum_{e=1}^{N_e} \rho_e \leq V, \\ & \text{‘AM distortion constraints’} \leq 0, \\ & 0 < \varepsilon \leq \rho_e \leq 1, \quad e = 1, \dots, N_e, \\ \text{with:} \quad & \mathbf{K}(\rho) \mathbf{u}_c = \mathbf{f}_c, \end{aligned} \tag{12}$$

where $c(\rho)$ represents compliance. $\mathbf{K}(\rho)$ is the structural stiffness matrix, \mathbf{f}_c and \mathbf{u}_c are the load vector and the displacement vector for the part performance simulation. ε is a lower bound on ρ set to prevent singularity and V is the maximum allowed volume fraction.

3.1. AM distortion constraints

The manufacturability of the design may be impaired by AM related distortions. Two distortion constraints are investigated in this paper. The first one is distortion during build, which could result in catastrophic collision of the recoater with the distorted product. The second is final distortion of the work-piece once released from the build plate, which could result in a product with out-of-spec dimensions.

3.1.1. Recoater collision

Recall that with every new layer deposition the build plate is lowered by a distance equal to the layer thickness and a new layer of powder is evenly spread over the working area with help of a roller or a rake, see Fig. 2. The

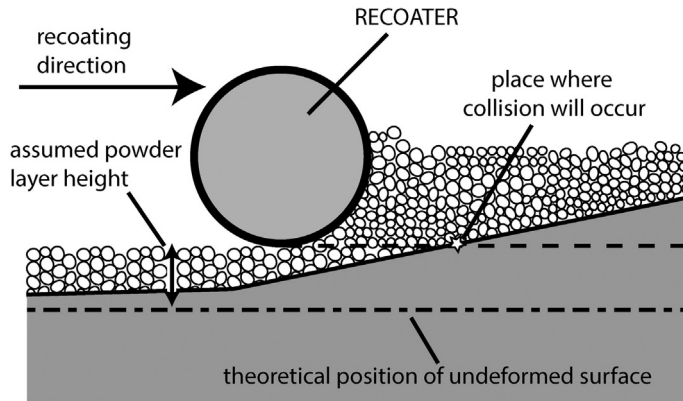


Fig. 2. Schematic recoater collision scenario.

recoater scans over the area and sweeps up a surplus of powder, assuring uniform constant powder layer thickness. In case of excessive shape distortions in the positive build direction, the recoater may collide with the part.

The danger of recoater collision is determined after the deposition of each layer, by monitoring the positive z -distortion of the top nodes of that layer. The constraint equations are then of the form:

$$\max(\varphi^{(i)}(\rho) \circ (\Delta \mathbf{u}_i^{(i)} \cdot \mathbf{e}_z)) - d_w \leq 0, \tag{13}$$

where multiplication of $\Delta \mathbf{u}_i^{(i)}$ with \mathbf{e}_z results in the vertical (z -)components of the displacement increments of the layer i top nodes after it has been deposited. The symbol ‘ \circ ’ denotes the Hadamard product, element-by-element multiplication of two arrays, which results in an array of the same dimension. The array $\varphi^{(i)}(\rho)$ contains nodal densities that are defined as an average of the densities of the currently active elements connected to a given node:

$$\varphi_k^{(i)}(\rho) = \frac{\mathbf{S}_k^{(i)T} \boldsymbol{\rho}^{(i)}}{N_k^{(i)}}, \tag{14}$$

where $\mathbf{S}_k^{(i)}$ selects the already deposited elements, which are connected to node k and $N_k^{(i)}$ is the number of active elements connected to node k . This is done to penalize only distortion of a solid part because a zero density means that no material is associated with the node of interest and no danger of collision exists. The allowable distortion d_w depends on the deposited layer thickness t and the relative density of the metal powder ρ_{pwr} :

$$d_w = \frac{t}{\rho_{\text{pwr}}}, \tag{15}$$

which accounts for the shrinkage of a powder layer of thickness d_w to a solid layer of thickness t . To make Eq. (13) differentiable, an envelope function [55] is used to approximate the max function:

$$g_i = \frac{1}{r} \log \left(\sum_{N^{(i)}} \exp \left(r \frac{\varphi^{(i)}(\rho) \circ (\Delta \mathbf{u}_i^{(i)} \cdot \mathbf{e}_z)}{d_w} \right) \right) - 1 \leq 0, \tag{16}$$

where $N^{(i)}$ is the number of nodes in the i th layer and r is a scaling parameter. When a higher value of r is chosen the function more closely approximates the max function but its derivatives are less smooth. Here the exponential function of the array is assumed to give an array of the exponentials of the components. The constraints of Eq. (16) may be either applied to every individual layer or aggregated in a single smooth max function over all layers. In this work, the latter option is chosen.

3.1.2. Global distortions

Distortion of a node is going to be measured with respect to its intended assembly position. Fig. 3 schematically depicts distortion during consecutive manufacturing stages. Due to the distortions, the theoretical assembly points

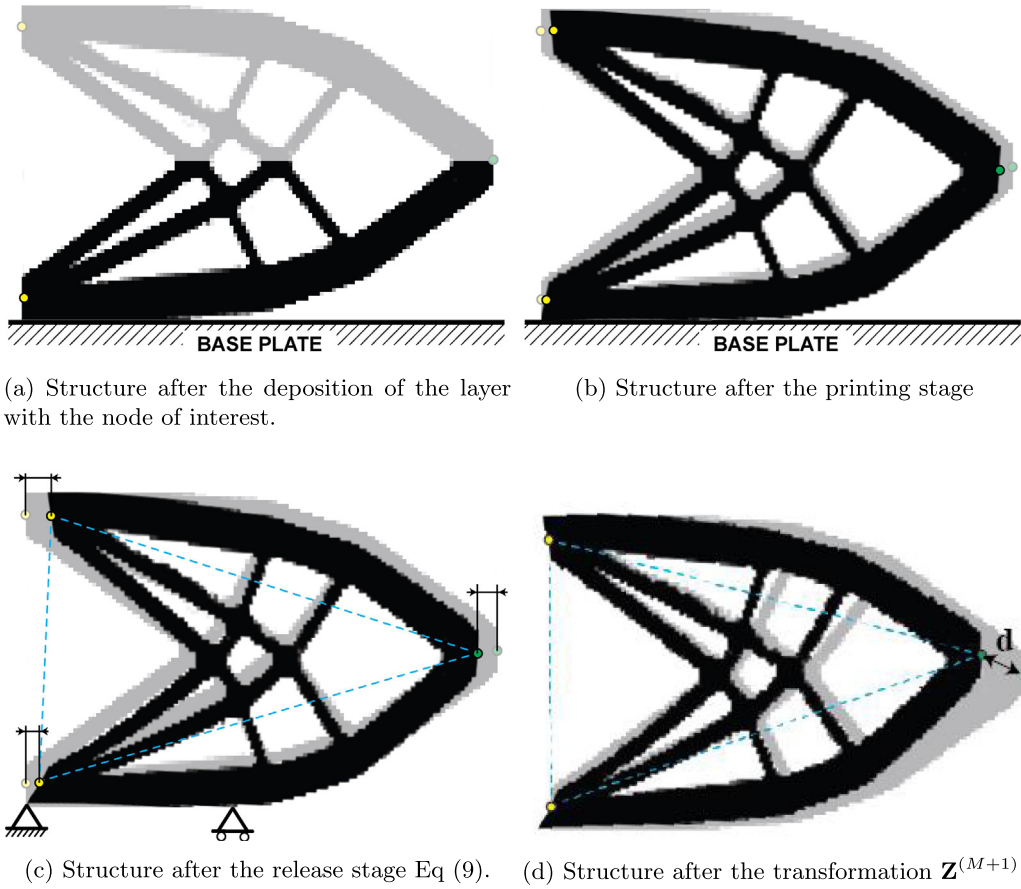


Fig. 3. Schematic of global distortion calculation. The theoretical shape is indicated in gray. (For interpretation of the references to color in this figure legend, the reader is referred to the web version of this article.)

(yellow dots) move away from their intended positions (yellow faded dots), therefore after the release stage, the whole structure has to be transformed in a way that puts the chosen nodes back to their designed position. The absolute position of the node of interest (green dot) is then measured with respect to its designed coordinates (green faded dot) after shifting the assembly nodes to their intended positions.

Distortion of a node consists of a series of displacement increments from each separate calculation step starting from the step in which the node got activated up to the final distortion from the release stage (Eqs. (8) and (9)). If the distortion of one node is to be measured and constrained relative to other nodes, that also distort during the printing process, a transformation has to be applied between a number of nodes, of which the first has been deposited as part of layer j . A final distortion vector is calculated in the form of:

$$\mathbf{d} = \sum_{i=j}^{M+1} \mathbf{R}^{(i)} (\mathbf{S}_g^{(i)} \Delta \mathbf{u}_f^{(i)} - \mathbf{S}_y^{(i)} \Delta \mathbf{u}_f^{(i)}) = \sum_{i=j}^{M+1} \mathbf{Z}^{(i)} \Delta \mathbf{u}_f^{(i)}, \tag{17}$$

where $\mathbf{S}_g^{(i)}$ is a selection matrix that chooses the node of interest (green), $\mathbf{S}_y^{(i)}$ is a selection matrix that chooses the bottom assembly node and after the subtraction translates the whole structure such that the yellow bottom node is back at its intended position (Fig. 3c). $\mathbf{R}^{(i)}$ is a rotation matrix that rotates the structure such that the top assembly node displacement x -component is equal to 0. Note that $\mathbf{R} = \mathbf{R}(\Delta \mathbf{u}_f)$ and that until the top yellow node has not yet been deposited the $\mathbf{R}^{(i)}$ matrix is simply the identity matrix. Moreover, if the yellow node is deposited before the constrained green node its displacement still contributes to the constraint function. $\mathbf{Z}^{(i)}$ is a transformation matrix

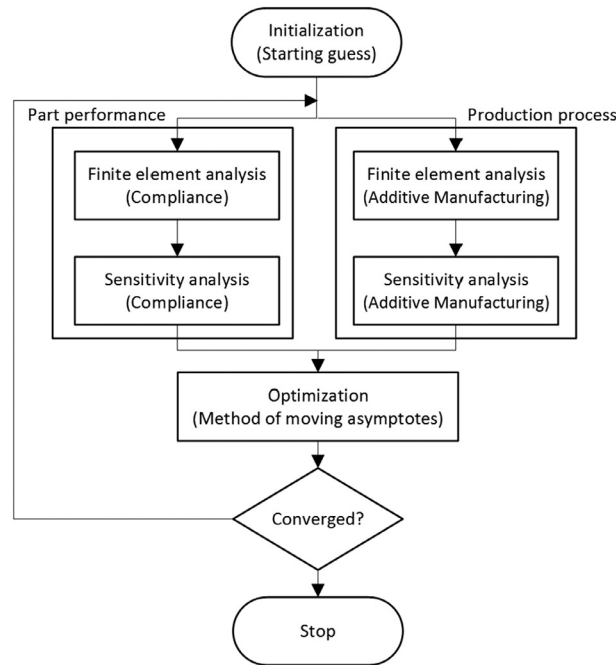


Fig. 4. Schematic illustration of the topology optimization algorithm that incorporates printing simulation.

that incorporates all of the above operations. This formulation can similarly be extended to 3D and to multiple nodes of interest.

The actual constraint g_d is a scalar function and is specified as:

$$g_d = \frac{1}{2} \mathbf{d}^T \mathbf{d} - \frac{1}{2} d_{\max}^2 \leq 0, \tag{18}$$

which signifies that the distortion of the considered node is constrained to a spherical tolerance region. If an ellipsoidal region is required, this can be realized by changing the first term to $\mathbf{d}^T \mathbf{A} \mathbf{d}$, whereas a p -norm may be used for a box-shaped region.

3.2. Constraint application

In every TO iteration a separate FEM printing simulation is performed. For this purpose, the numerical model described in Section 2 is used. The simulation provides information on the degree of distortion and the possible printing constraint violations. Moreover, to find a change in design variables that minimizes the objective function while satisfying the constraints, the sensitivities of these constraints with respect to the design densities have to be calculated. For this purpose, the adjoint method is suitable [56], given the large ratio of design variables versus responses. The derivation of the adjoint equations is given in Appendix.

The constraint functions and their sensitivities are incorporated into the TO algorithm in accordance with the flowchart in Fig. 4. As depicted, two parallel numerical calculations are required for each optimization iteration. The AM simulation and its sensitivity calculation is the most time consuming one due to the sequential nature of the model. However, Munro et al. [52] have shown that the steps of this manufacturing simulation can be evaluated in parallel and thereby overall computation time can be decreased significantly. To prevent checkerboard pattern solutions, density filtering is applied [54]. The sensitivities for filtered densities are consistently transformed to unfiltered densities and then supplied to the optimizer. The Method of Moving Asymptotes [57] is applied to perform the constrained optimization. Finally, a convergence check is done and the algorithm proceeds to the next iteration or stops.

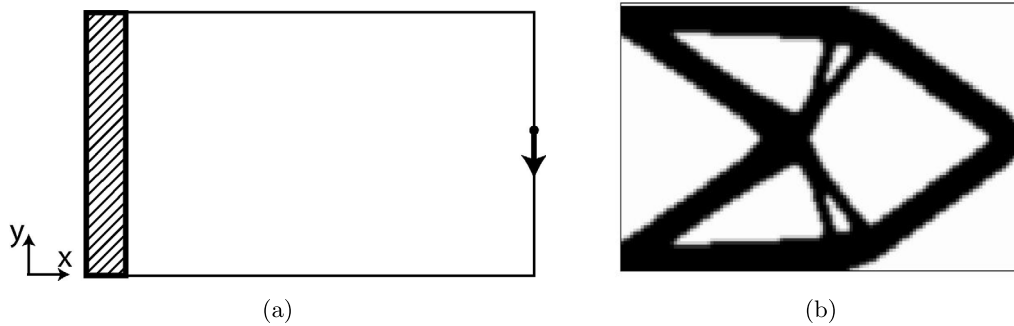


Fig. 5. Depiction of (a) the design domain with boundary conditions and (b) obtained part layout for compliance minimization without printing constraints.

4. Results

The scheme proposed in Section 3 for topology optimization and the calculation of adjoint sensitivities is applied in this section to optimizations with different combinations of additive manufacturing related constraints on both 2D and 3D bracket examples. The case investigated in optimization is a bracket that is fixed on one side and loaded on the other side. The numerical algorithm is parallelized using OpenMP and simulations are always set to run on 8 cores of a 12-core machine, Intel(R) Xeon(R) CPU E5-2690 v3 @ 2.60 GHz.

4.1. 2D examples

In the 2D examples, a rectangular design domain is considered that is discretized by 120×80 bilinear quadrilateral elements of 1×1 mm with 2×2 Gaussian integration scheme. Compliance is minimized for the structure when it is supported on the left side and a vertical load is applied in the center of the right edge, see Fig. 5(a). The material properties are representative of Ti6Al4V with Young's modulus $E = 110$ GPa and Poisson's ratio $\nu = 0.342$. The prescribed load f_c directed in the negative y -direction has a magnitude of 1000 N. A plane strain deformation is assumed in the simulation. The maximum volume fraction is set to 40%. The density filter radius is set to 1.5 mm.

The prescribed inherent strain $\boldsymbol{\varepsilon}_{inh} = [0.00598, 0, 0]$ in Eq. (4), following the Voigt notation. The value is chosen to correspond to the x -component of the thermal contraction of Ti6Al4V when cooled down from 800 °C to 150 °C which is in accordance with values assumed by other researchers [58,59]. The printing simulation is performed with element layers of 1 mm thickness per step, which contain the lumped effect of 20 printed layers, each with a thickness of 50 μm . Convergence for the optimization is assumed to be reached when the relative change in compliance averaged over the last 3 iterations is less than 10^{-5} and all constraints are satisfied.

As a reference case, a compliance minimization without any printing constraint is performed. It results in the symmetric shape shown in Fig. 5(b). The obtained compliance value is $c = 345$ mJ. The optimization required 133 iterations to converge which took 7 min and 5 s in our implementation. The printing simulation of this configuration reveals extensive recoater collision, which is shown in Fig. 6. The global distortion of the reference point amounts to 0.61 mm after the separation from the base plate.

To show the optimization capabilities, 3 types of optimization with 9 different cases are presented. The applied constraint values in these optimization settings are tabulated in Table 1. First, an optimization with the recoater collision constraint is carried out. It is followed by four optimizations for different values of d_{max} with the global distortion constraint prescribed on the node where the load is applied. Finally, optimizations for four different values of d_{max} , combined with the recoater collision constraint are done.

4.2. Recoater collision

Recoater collision occurs when the top nodal row of a newly deposited layer distorts upwards in printing direction, above a critical value. In the investigated case, a layer thickness of $t = 50$ μm and relative powder density ρ_{pwr} equal to 50% are assumed, consequently the collision threshold d_w according to Eq. (13) has been set to 100 μm .

Table 1
Constraints applied in different optimization cases of the 2D example.

d_{\max} (mm)	d_w (mm)	Section
–	–	4.1
–	0.1	4.2
0.5	–	4.3
0.2	–	4.3
0.1	–	4.3
0.05	–	4.3
0.5	0.1	4.4
0.2	0.1	4.4
0.1	0.1	4.4
0.05	0.1	4.4

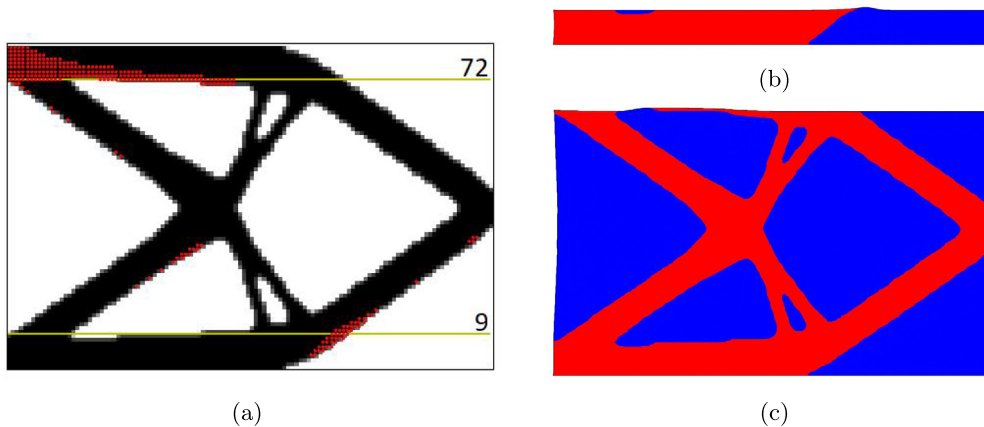


Fig. 6. Recoater collision for design without printing constraint: (a) nodes for which collision will occur (marked red). Deformed configuration after (b) step number 9 and (c) step number 72, red color indicates material and blue void. (For interpretation of the references to color in this figure legend, the reader is referred to the web version of this article.)

The regularization parameter r in Eq. (16) is set to 25 and the constraint has been aggregated for all of the layers into a single value.

Given an element height of 1 mm and a layer thickness of 50 μm , 20 layers are lumped in a single row of elements for the distortion analysis. For the deposition of every row of elements a separate solution step is required. Therefore, for the considered bracket each AM printing simulation takes 80 steps in total.

From the full printing simulation it is observed that the reference design, as obtained from compliance minimization only, would result in recoater collision for the nodes depicted in Fig. 6(a). It is worth recalling that in case of the recoater collision, distortions are multiplied by the nodal densities (see Eq. (15)), so only nodes which belong to the part can violate the constraint.

There are several regions where the recoater will collide with the part. The first one is located in the bottom right corner, where the thick member starts ascending. This is caused by the horizontal length of the structure for these layers and their significant distance to the base plate connection. Moreover, at the end of the same member, a collision can be observed near the tip where the load is to be applied and on the sides of some of the inside members. The largest area, where recoater collision occurs, is located in the top left corner where long material layers exist with almost no support to the base plate and with a void beneath the member. Two snapshots of the distortion at intermediate build stages after 9 and 72 printing steps are depicted in Fig. 6(b) and (c), which clearly indicate the distortion in the build direction.

The result of TO with the recoater collision constraint is presented in Fig. 7. For this structure, the constraint is nowhere violated. It can be noticed that the bottom member of the structure, where previously collision occurred, becomes thinner in the location where the part starts to ascend (marked with A). The reduction of horizontal length for layers where collision happened could prevent it and therefore the material has been removed. Moreover, an

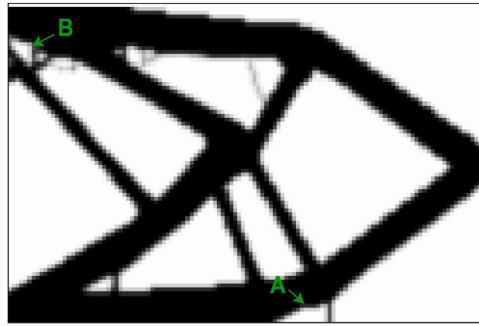


Fig. 7. Design obtained from compliance minimization with recoater collision constraint.

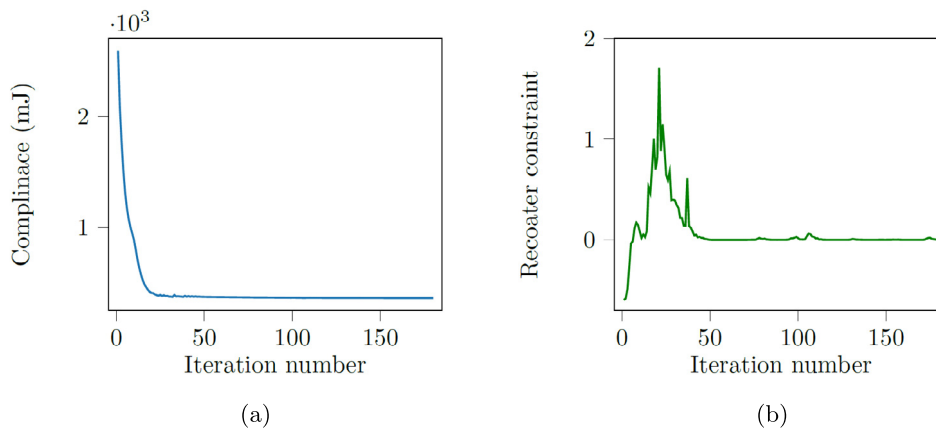


Fig. 8. Compliance (a) and constraint (b) history as a function of iteration for the optimization with recoater collision constraint.

additional small column is introduced which connects it to the base plate. Since it has no connection with the left edge, its only function is to limit distortion during printing by adding mechanical support. Its small cross-section resembles the supports used in actual powder bed AM processes. All the external members have a slightly reduced width and additional internal members have been introduced. The horizontal length of layers on the top member has been shortened by a change of the inclination angle which results in a shorter top edge and a void region (marked with B) that cuts into it from below. Some internal supporting material can also be observed in this region. Moreover, the vertical symmetry of the part which is observed in Fig. 6 has been broken due to nonuniform distribution of the distortions. Inner supporting branches have moved, to compensate for the influence of changes introduced by the collision constraint application.

The evolutions of compliance and constraint function are plotted against optimization iterations in Fig. 8. Convergence has been obtained after 180 iterations and the final compliance is equal to 363 mJ which is 5.2% higher than that of the reference case. The computational time is 41 min and 6 s which is almost 6 times longer than that of the reference case. This is due to the fact that a single optimization iteration now requires 80 steps of printing simulation and adjoint sensitivity calculation, in addition to the single step compliance simulation. The constraint plot indicates collision during early iterations of the optimization but almost no violation of the constraint afterwards. The small peak after 100 iterations indicates that the design violated the constraint and that the solution was in the infeasible space for a few iterations. This is not uncommon behavior for optimization problems with nonlinear constraints when the constraint is active. The volume constraint, which is not shown, is preserved for all of the optimization iterations.

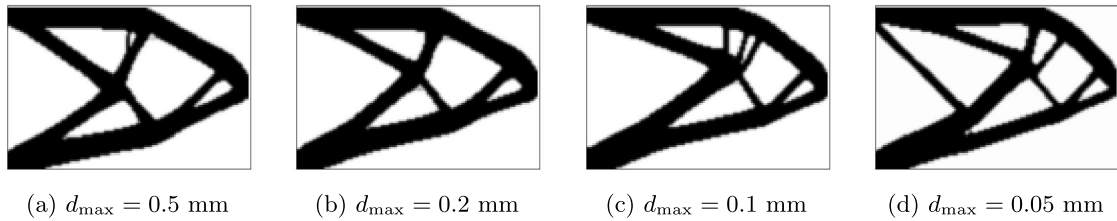


Fig. 9. Designs obtained for compliance minimization for selected values of loaded point distortion constraint d_{\max} .

Table 2

Results for optimization with and without distortion constraint including the release stage.

d_{\max} (mm)	Compliance (mJ)	Iterations	Time (hh:mm:ss)
–	345	133	0:07:05
0.5	347	137	0:30:02
0.2	354	286	1:03:37
0.1	362	310	1:08:43
0.05	369	309	1:07:59

4.3. Global distortion

As a second optimization case, a constraint on global distortion, Eq. (18), has been imposed on the node where the load is applied (see Fig. 5a). This distortion constraint measures the state of the structure after the entire printing process, after separation from the base plate and transformation to the intended position. Printing distortion is due to thermal contraction of the layer containing that node and the thermal contraction of all subsequent layers during the printing stage. Recall that thermal contractions that are constrained due to clamping of the work-piece to the base plate give rise to residual stresses. Consequently, when the part is released from the base plate, an additional distortion is generated due to the relaxation of these residual stresses.

The constraint is set on the final position of the loaded node, measured with respect to its intended assembly position (see Fig. 3). Optimization has been performed for four values of allowable distortion: d_{\max} equal to 0.5, 0.2, 0.1 and 0.05 mm. In the reference design (see Fig. 5b), a distortion $d = 0.61$ mm is observed for the node under consideration.

The designs obtained with selected values of d_{\max} are depicted in Fig. 9. It can be observed that with a decreasing level of allowed distortion the bottom member becomes more straight and thinner while the number of internal members and therefore the geometric complexity increases. The bottom member that becomes straight with the increasing strictness of the constraint, has little connection to the base plate. In that way, distortions generated during release are reduced because the number of degrees of freedom, for which the released reaction forces accumulate, is less. When compared to the outcome of pure compliance with no printing constraints, the designs feature more complex topologies and the vertical symmetry is again broken.

The results of the performed optimizations, the achieved compliance value, the number of required optimization iterations, and the required computational time are summarized in Table 2. As anticipated, the compliance value increases as the constraint becomes stricter. The same happens for the number of iterations required for convergence. Consequently, the calculation time increases substantially.

In Fig. 10, the evolution of compliance and constraint for the different global distortion constraint cases is presented. Compliance plots are almost on top of each other, which indicates similar convergence behaviors. In the distortion constraint plot, a few characteristic peaks may be observed at the earlier iterations for all of the plots. It means that for the optimizer it is harder to remain in the feasible space but after 50 iterations the behavior is quite smooth.

In Fig. 11, the displacement field for constraint value $d_{\max} = 0.05$ mm is depicted. It is obtained by performing a printing simulation for the whole domain including the void region. This is followed by a postprocessing step where elements with densities below 0.8 are removed to show the relevant displacement field for the structure only. The plots confirm that the constrained upper left corner node as well as the node to which the force is applied is at

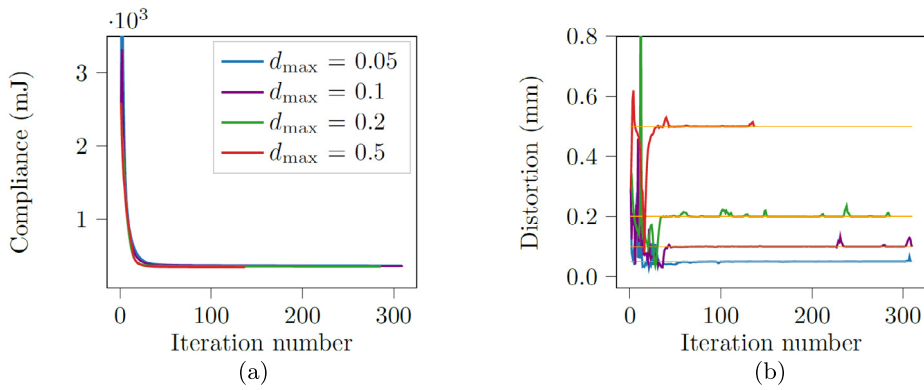


Fig. 10. Compliance (a) and distortion (b) history as a function of iterations for optimization with a distortion constraint.

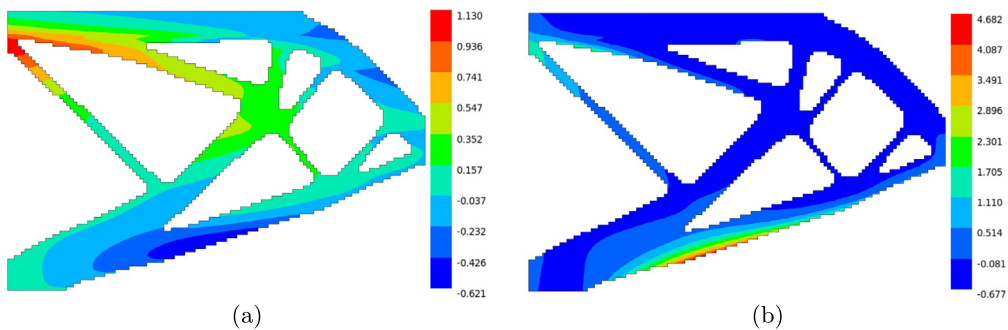


Fig. 11. Displacement plots (in mm) of the shape obtained for $d_{max} = 0.05$ mm after release: displacement components in x -direction (a) and y -direction (b).

the intended positions. Large parts of the structure that are not included in the constraint show distortions in excess of 0.05 mm and even up to 4.7 mm. The positive displacements in the x -direction are this time more severe and go up to 1.1 mm for the thin member in the top left corner. The positive displacements in the y -direction have been reduced due to the reduction of the layer lengths and now the highest value is 4.7 mm, whereas for the rest of the part displacements in the y -direction are rather mild.

4.3.1. Relevance of the release stage

In the previous section, an assumption has been made that right after the printing stage the part is separated from the base plate. In metal additive manufacturing, it is often the case that heat treatment is done after the printing stage [60]. Post fabrication heat treatment is performed to increase the part homogeneity, remove possible voids, and to reduce accumulated residual stresses. If most of the stresses are relaxed due to the heat treatment, little additional distortions occur when the part is released from the base plate.

An additional optimization is performed, where simulation is stopped after the last printing step, omitting the distortion at part release and only applying the transformation of nodes to their intended assembly position. This mimics the situation where heat treatment, that relaxes all the residual stresses, precedes part release. Hence no further distortions occur during the release stage. Optimization for a part that undergoes a full stress relief heat treatment is therefore comparable to an optimization where only the building stage is simulated without the release stage. The constraint is again set on the final position of the loaded node, measured with respect to its designed assembly position (see Fig. 3, Eq. (17)). Optimization is performed for a value of allowable distortion, $d_{max} = 0.05$ mm. In the reference design, i.e. compliance minimization without any printing constraint, a distortion value of $d \approx 0.3$ mm is observed for the node under consideration after the last printing step, before the release step.

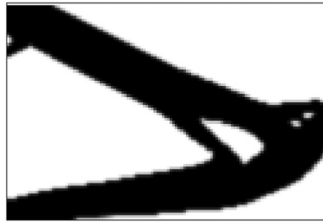


Fig. 12. Design obtained for compliance minimization considering distortions during printing only and full stress relief before release, for $d_{\max} = 0.05$ mm.

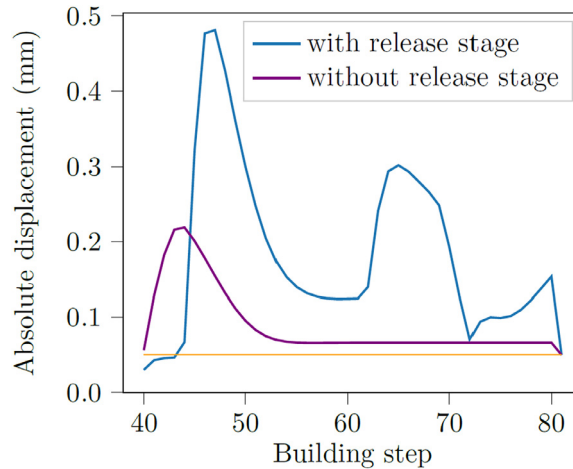


Fig. 13. Comparison of the evolutions of distortion of the constrained node for the optimized structures as a function of build step. The final step (81) represents the release from the base plate. The orange line indicates the allowed distortion. (For interpretation of the references to color in this figure legend, the reader is referred to the web version of this article.)

The obtained design (see Fig. 12) significantly differs from that obtained when distortion during release is taken into account (see Fig. 9(d)). The top member becomes more straight and points in the direction of the constrained node. The reason is presumably to limit the amount of material above the node of interest. A material layer above any given point leads to an increase in distortions due to the thermal shrinkage that is introduced with its deposition. Therefore, the optimizer tends to avoid material placement above the constrained node. Moreover, the amount of material in contact with the base plate increases. Not taking the release stage into account means that accumulation of reaction forces at the base plate has no influence on distortions.

In case of an optimization that incorporates both printing and release stages, distortions that accumulate in the growth stage can be compensated in the final release step. To show this, the distortions of the node of interest as a function of printing steps are plotted in Fig. 13, for the optimized designs obtained in both cases. It can be seen that for the simulation, which includes the distortions during the release stage, in the final release step the distortions drop down from over 0.15 mm to 0.05 mm due to the release from the base. In case of the simulation without distortions during the release stage (i.e. with heat treatment assumed) distortion of the constrained node remains constant from the 55th building step while in the final increment only the transformation to the assembly position is applied. So the two scenarios (i.e. with and without heat treatment) lead to different designs that exploit different distortion reduction mechanisms.

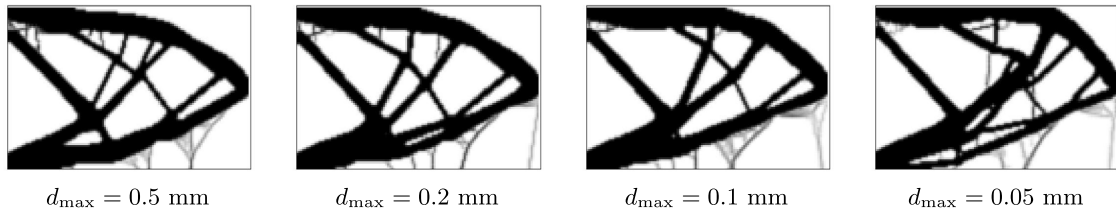
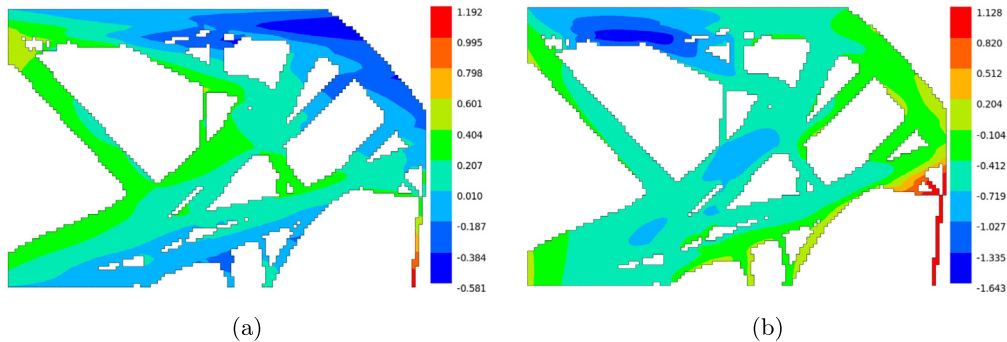
4.4. Recoater collision and global distortion combined

It remains to apply the recoater collision and the global distortion constraints simultaneously. Optimizations have been performed for d_{\max} again equal to 0.05 and 0.1, 0.2 and 0.5 mm. All of them are combined with the recoater collision threshold $d_w = 100 \mu\text{m}$.

Table 3

Results for optimization with combined distortion and recoater collision constraints.

d_{\max} (mm)	d_w (mm)	Compliance (mJ)	Iteration	Time (hh:mm:ss)
–	–	345	133	0:07:05
0.5	0.1	371	397	2:07:52
0.2	0.1	379	639	3:13:33
0.1	0.1	387	329	1:42:27
0.05	0.1	410	202	1:01:41

**Fig. 14.** Designs obtained with a constraint on final distortion with different values of allowed distortion d_{\max} combined with recoater collision margin d_w .**Fig. 15.** Displacement plots (in mm) of the shape obtained for $d_{\max} = 0.05$ mm after release: displacement components in x -direction (a) and y -direction (b).

The obtained compliance values and other optimization data are tabulated in Table 3. It can still be observed that the value of the objective increases with the strictness of the constraint, but the number of required iterations no longer follows this trend. This may be due to the increased nonlinearity of the problem. The longest calculation time occurs for the case with $d_{\max} = 0.2$ mm and $d_w = 0.1$ mm, which took over 3 h. This is caused by the large number of iterations (639) that were required for convergence. During the optimization the design repeatedly strays between regions of distortion infeasibility and recoater collision infeasibility. For d_{\max} equal 0.1 and 0.05 mm the value of the objective increased by 12.2% and 18.9% respectively when compared to the reference case.

There is some similarity between designs with the same d_{\max} for optimizations with and without the recoater collision constraints (see Figs. 9 vs. 14), but overall the shapes which include both constraints are more complex. For both cases, the same straightening of the lower ascending member can be observed. Furthermore, the irregularity of member thickness is much more pronounced than before. Finally, many thin structures that either connect the part with the base plate or interconnect the members themselves emerge. These structures resemble support structures that are typically used in 3D printing. Many of the supports are still grayish, i.e. have intermediate density values, which indicates that the full stiffness of solid material is not needed in this case to achieve the desired distortion-reducing effect. This is in line with the fact that for support structures in practice lattice structures are often used. The load carrying members of the part itself have converged to a clear solid/void layout.

Visual inspection of displacement plots for $d_{\max} = 0.05$ mm in Fig. 15 again confirms that the constrained nodes stay in place (within the allowed tolerance). The highest distortions occur for the thin support in the bottom

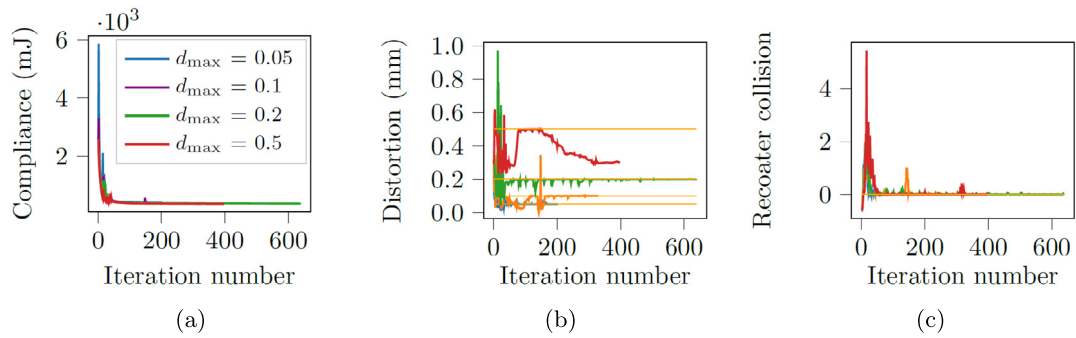


Fig. 16. Compliance (a), distortion (b) and recoater collision (c) as a function of iteration for optimization with a distortion and recoater constraint, orange line indicates constraints. (For interpretation of the references to color in this figure legend, the reader is referred to the web version of this article.)

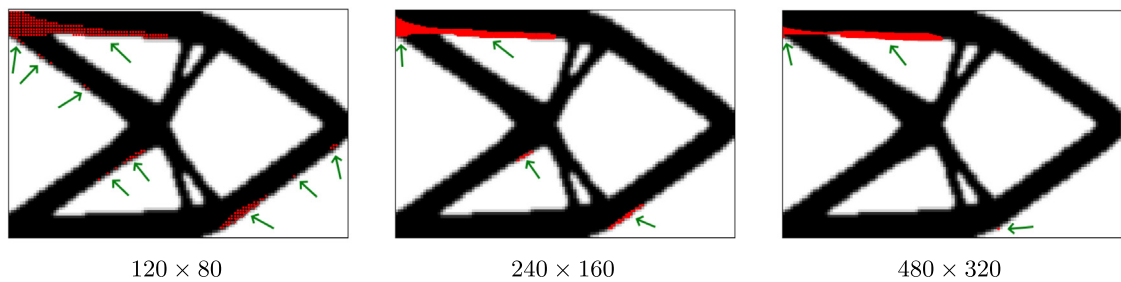


Fig. 17. Recoater collision for different domain discretizations. Green arrows indicate regions for which collision occurs.

right corner. These displacements are caused by the release stage where the bottom of the member is freed, and in consequence, it warps in counter-clockwise direction. Note that this support distortion does not affect the global distortion constraint, since that is aimed at controlling the loaded node position in assembled configuration. The overall part distortions are smaller compared to the case without the recoater collision (see Fig. 11). The reason is that recoater collision is a constraint that affects all layers and therefore the distortions in the whole structure are reduced.

The objective and constraint history plots (see Fig. 16) again show that at the beginning, the optimizer has problems with remaining in a feasible space (spikes in the plots), but after 200 iterations the plots are rather smooth. The biggest drop of the objective function occurs in the first couple of dozens of iterations. Moreover, the optimization always converges to a feasible solution.

4.5. Mesh size dependence

In this section, the influence of the mesh size on the obtained results is investigated. The same design layout will be printed with different mesh resolutions and therefore a different number of material layers is lumped into a single element layer. The reference design layout depicted in Fig. 5b will be printed to check how the mesh size influences constraints, i.e. recoater collision and nodal distortions. Mesh sizes of 0.5×0.5 mm and 0.25×0.25 mm were used, resulting in domains discretized by 240×160 and 480×320 elements respectively.

In Fig. 17, the nodes for which recoater collision occurs are depicted. It can be observed that as the resolution increases, the region for which collision occurs decreases. This happens because with the decrease of the element size fewer layers are lumped within a single element layer, which leads to smaller inherent strain energy deposited in a single step and therefore to lower incremental displacements. For the distortions of the node of interest after the release stage, displacements of 0.61 mm, 0.67 mm and 0.69 mm were observed for the domains of 120×80 , 240×160 and 480×320 elements, which is a relatively small difference.

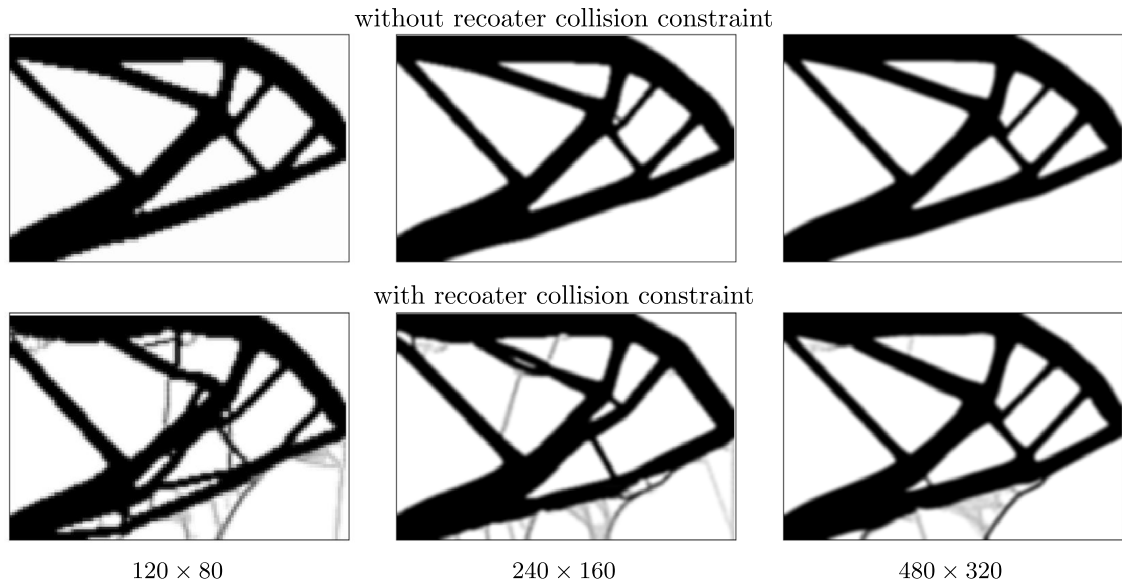


Fig. 18. Optimal designs for different domain discretizations.

The influence of the mesh size is here investigated on two examples, both for the final deformation of the node of interest constrained to 0.05 mm, without and with the recoater collision constraint. The same discretization variations are investigated: 120×80 , 240×160 and 480×320 . The applied density filter is always set to 1.5 mm to enforce the same minimum physical feature size between the examples.

Optimizations without the recoater collision constraint required 309, 276 and 191 iterations for convergence, whereas optimizations with the recoater collision constraint required 202, 234 and 184 iterations following the order from the coarsest to the most refined mesh. The obtained designs are presented in Fig. 18. Although the designs are not identical the similarity is undeniable. Interestingly, designs with recoater collision constraint start to resemble the designs with only distortion constraint as the resolution increases. This is due to the fact that the recoater collision constraint becomes less critical with the increase of the mesh resolution as Fig. 17 indicates. Moreover, the obtained shapes suggest that in some cases recoater collision could be prevented by proper placement of the supports only.

4.6. 3D examples

To demonstrate the application potential of the proposed TO formulation for 3D design cases, optimizations have been performed for a 3D structure, using the same minimum compliance objective as the above 2D bracket. This way it is possible to check whether trends that are seen in 2D also occur in 3D. The design domain used for optimization is composed of $80 \times 40 \times 40$ elements of $1 \times 1 \times 1$ mm standard trilinear hexahedral elements with Gaussian integration scheme. Compliance is minimized for the structure that is supported on the left side and the load is applied vertically along a horizontal line going through the middle of the right side (see Fig. 19(a)). During the printing stage, the bottom is fully constrained (see Fig. 19(b)) and in the release stage the bottom left edge is constrained in x and z -directions, the top edge is constrained in the x -direction and the middle node of the bottom left edge is fully suppressed (see Fig. 19(c)).

The material considered is Ti6Al4V with the same properties as for the 2D cases and the inherent strain applied in simulations is $\epsilon_{inh} = [0.00299, 0.00299, 0, 0, 0, 0]$ which would be an average value for the lumped method with a rotational scanning strategy. So the same inherent strain as in 2D examples is now applied but with rotation in the x - y plane. For all the cases the maximum volume fraction is set to 40% and the density filter radius is set to 1.5 mm. The convergence criterion is again set to the relative change of the objective function averaged over the last 3 iterations to be lower than 10^{-5} while constraints are satisfied.

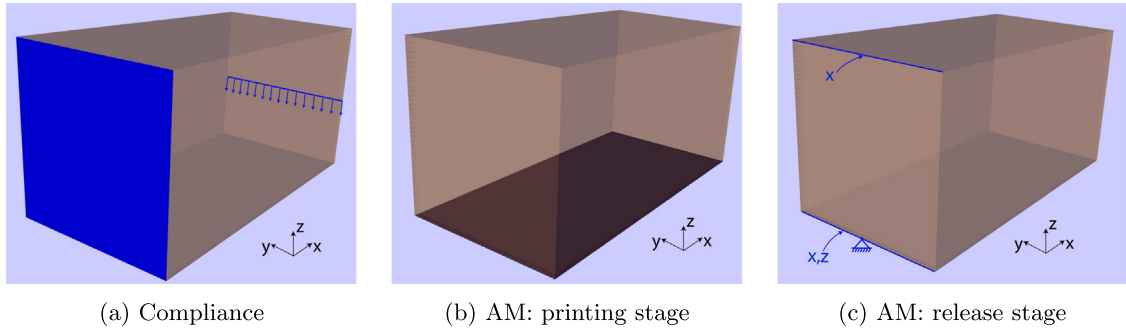


Fig. 19. Boundary conditions for different stages of simulation.

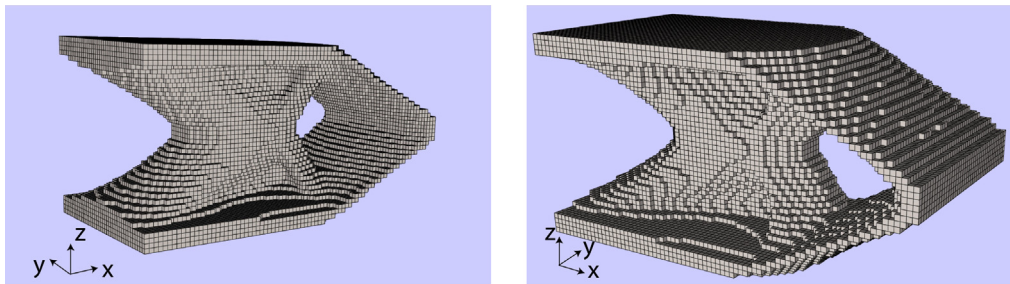


Fig. 20. Reference design obtained from compliance minimization.

Table 4
3D topological optimization results with different additive manufacturing constraints.

d_{max} (mm)	d_w (mm)	Compliance (J)	Iteration	Time (hh:mm:ss)
–	–	29.9	182	9:24:12
–	0.1	30.3	683	276:30:54
0.1	–	32.6	327	110:20:07
0.1	0.1	33.1	308	184:11:02

The compliance minimization with only the volume constraint is performed as a reference case. The final objective function value is 29.9 J and convergence is reached after 182 iterations. In total the optimization took over 9 h. The obtained shape is presented in Fig. 20. We note in passing that only the elements that have density above or equal to 0.9 are plotted.

Three 3D optimization cases will be presented. The first concentrates on the recoater collision constraint. This is followed by optimizations with d_{max} set to 0.1 mm, with and without the recoater collision. The global distortion constraint is formulated such that it limits the distortion of all loaded nodes to d_{max} . For this purpose, the distortions of loaded nodes are gathered into a single p -norm function:

$$g_p = \sqrt[p_n]{\mathbf{1}^T \left| \sum_{j=1}^{M+1} \mathbf{Z}^{(j)} \Delta \mathbf{u}^{(j)} \right|^{p_n}}. \tag{19}$$

The max-norm is approximated by setting $p_n = 7$.

The results of the performed optimizations are summarized in Table 4. The trend of increase of the objective value with the increase in strictness of the constraints is again noticed. Compared to the 2D examples the number of required iterations is roughly similar. Nevertheless, the calculation time increased significantly. The longest calculation time is needed when only the recoater collision constraint is applied. In total, it takes 11 and a half days, which is a substantial amount of time. Note that the present implementation is a research code and further efficiency gains through optimization and parallelization are possible. Since the layer additions in the considered

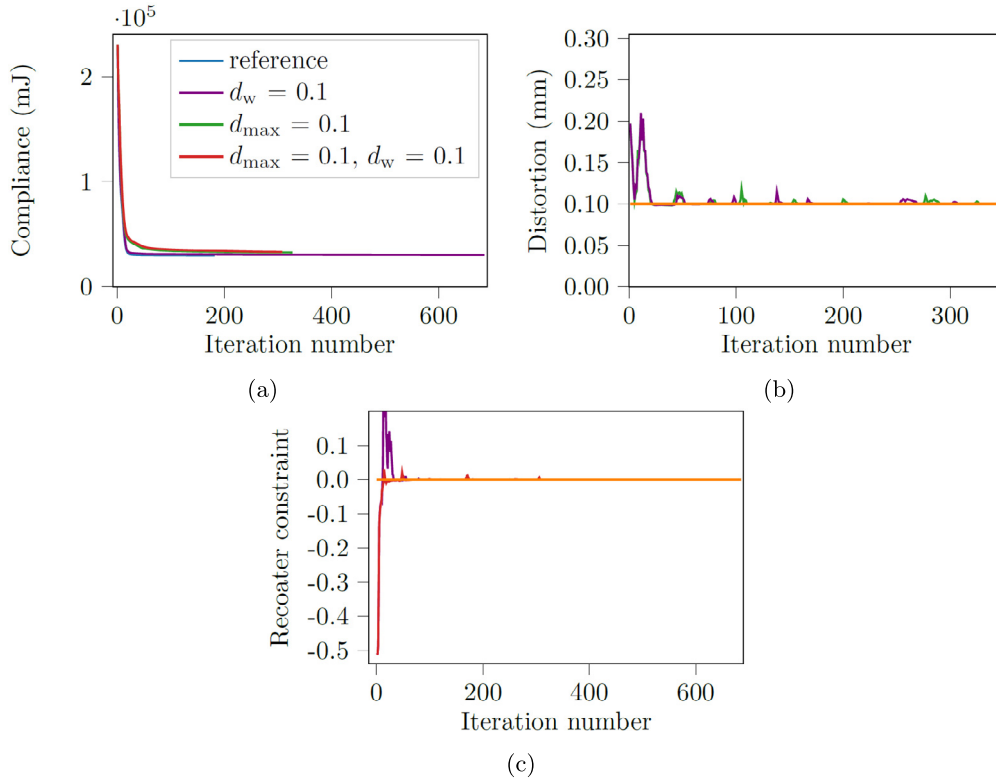


Fig. 21. Compliance (a) and constraints (b) and (c) as a function of iterations for optimization with Additive Manufacturing constraints.

modeling approach can be computed independently, at least a factor 10 reduction in computation time seems possible with the parallel solution approach of Munro et al. [52].

Convergence plots for all 3D optimization cases are presented in Fig. 21. Most of the objective function reduction occurs in the first 50 increments, and the same goes for jumps in distortion and collision constraints. This suggests that the applied convergence criterion might be relaxed in order to reduce the computation time. The constraints are preserved for most of the iterations and their iteration histories resemble those in the convergence plots from optimization in 2D.

4.6.1. Recoater collision

The same conditions as for 2D have to occur for recoater collision to happen. Therefore, d_w is set to $100 \mu\text{m}$. Again the parameter r in Eq. (16) is set to 25 and the constraint has been aggregated for all of the layers into a single function; since the domain height is 40 elements, 40 separate deposition steps are gathered. The printing simulation of the reference shape shows that collision occurs for nodes marked by red dots in Fig. 22. In total 2153 nodes violate the constraint and as it can be observed they are all located in the top of the structure. The highest distortion in the z -direction is 0.33 mm which exceeds the threshold.

The design obtained with the application of the recoater collision constraint is presented in Fig. 23. When compared to the reference case the shapes of the inner members, shapes are more complex and the symmetry of the part in the z -direction is broken. Additional members have been added, marked with A, to support the top of the structure where the collision occurs in the reference design. The front of the structure did hardly change, which is according to expectation since the printing simulation revealed not recoater collision in this region.

4.6.2. Distortion constraint

The maximal distortion of constrained nodes in case of printing the reference design is found to be 0.66 mm. The allowed maximum distortion d_{max} is set to 0.1 mm, and the resulting design that meets this constraint is presented in

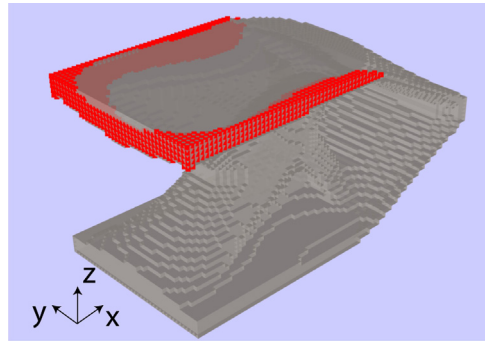


Fig. 22. Recoater collision for the reference design.

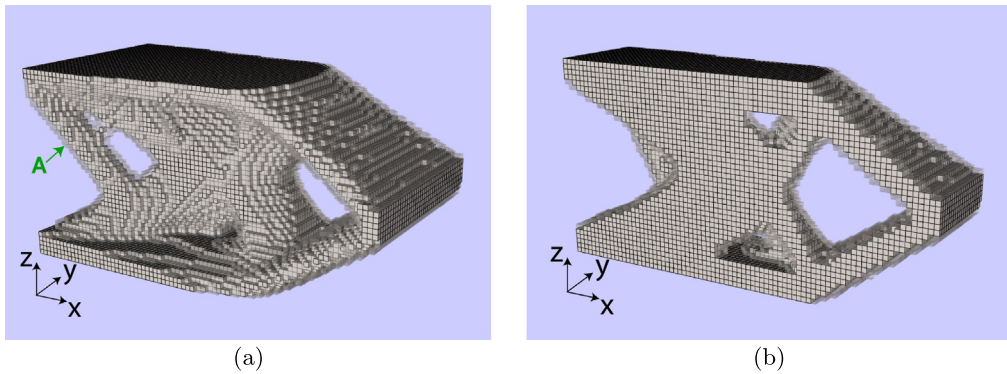


Fig. 23. Shape obtained from compliance minimization with recoater collision constraint. Full shape (a) and shape cut in half at $y = 20$ mm (b).

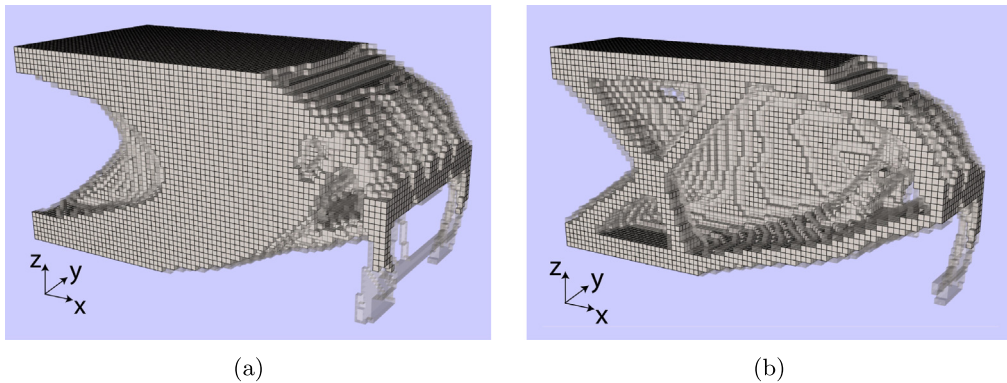


Fig. 24. Full shape (a) and shape cut in half (b) obtained for minimization of compliance with distortions constraints.

In Fig. 24 only elements that have density above or equal to 90% are plotted as full, while the transparent elements are those with a density that is between 20% and 90%. This allows for visualization of possible low-density support structures, as observed in the 2D case.

The optimizer proposes a hollow structure. This may cause practical difficulties with powder evacuation but controlling this aspect is beyond the scope of this study, and the interested reader is referred to [61] and the references therein. Two fully dense pillars in the corners of the design domain have been introduced, which act as supports. The same straightening of the bottom as for the 2D examples occurs.

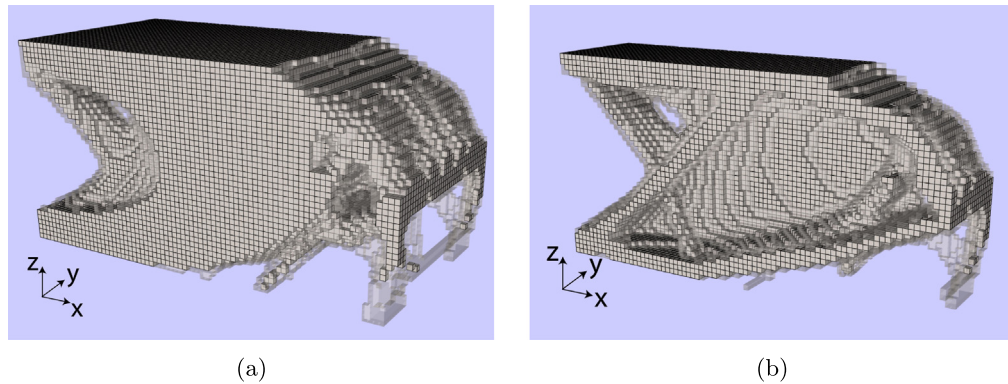


Fig. 25. Full shape (a) and shape cut in half (b) obtained for minimization of compliance with distortion constraints combined with the recoater collision constraint.

4.6.3. Distortion and recoater collision constraints combined

The constraints studied separately in the two preceding sections are now combined in a single optimization problem imposing both distortion and recoater collision constraints. The shape obtained from the optimization is presented in Fig. 25. The obtained design resembles that obtained with only the constraint on final distortion applied. Again, a shell-like hollow structure with thinner inner members that were moved to the left side can be observed. More complex support structures emerge, when compared to the previous example, which matches with the trend observed in 2D for the cases with both constraints applied (see Fig. 14). A small pillar is introduced close to where the structure starts to ascend from the base plate.

5. Conclusions

A Topology Optimization scheme with distortion constraints, that assure manufacturability through powder bed based Additive Manufacturing, has been presented. The main goal is to apply constraints that, when satisfied, prevent unwanted shape distortions during the production while the structure is still able to perform its objective. Given this focus, other printability criteria were excluded to study the influence of the distortion constraints. Constraints were evaluated by an inherent strain based 3D printing model. A SIMP based topological optimization scheme was utilized. The gradients of the constraint functions with respect to the design variables need to be calculated. For this purpose, a derivation of sensitivities of distortions has been formulated based on the adjoint method.

Two different production constraints have been investigated: prevention of recoater collision and limitation of global shape distortions. Simulation of printing of the reference design predicts recoater collision to occur in many instances during the building of the structure and the built structure is predicted to endure considerable distortion. When the optimization is performed with AM constraints, the recoater collisions are completely prevented as are excessive final distortion of nodes of interest. The optimized designs feature many auxiliary support structures, which aim at facilitating production, rather than enhancing the parts structural performance. Auxiliary structures often are composed of semi-dense material, which can be interpreted as lattice-type support structures routinely used in practice. In case of a global distortion constraint, the optimization is found to compensate distortions by alteration of part shape and by adding supports. Moreover, it has been shown that distortions generated during the printing stage are compensated by the additional distortions generated when the part is released from the base plate.

The applicability and effectiveness of the method have been illustrated both in 2D and 3D. Optimizations of a bracket in 3D including the proposed distortion constraints are characterized by the creation of box-like structures, in contrast to a bulky central structure seen in the conventional compliance minimization result. The total optimization time for 3D was in a range of days, which is still reasonable because it involves a transient numerical model. Moreover, there is potential to accelerate the present implementation.

The addition of Additive Manufacturing constraints to SIMP based Topology Optimization expectedly results in a modest increase of the compliance objective by 4 to 29%, depending on the strictness of the constraints. However, given the high cost of failure at a late stage of the design- or printing process, it can be highly recommended to include these crucial constraints in design for AM.

Declaration of competing interest

The authors declare that they have no known competing financial interests or personal relationships that could have appeared to influence the work reported in this paper.

Acknowledgments

This research was carried out under project number S12.7.14549b in the framework of the Metals for Additive Manufacturing Partnership Program of the Materials innovation institute M2i (www.m2i.nl) and the Netherlands Organization for Scientific Research (www.nwo.nl). The authors thank Krister Svanberg for use of the MMA optimizer.

Appendix. Sensitivity of the constraints

The sensitivities of the collision constraints and the distortion constraint are all determined by the adjoint method since this has considerable advantages in implementation.

A.1. Sensitivity of the recoater collision constraint

To obtain the sensitivity of the collision constraint, g_i of Eq. (16) is augmented with Eq. (6):

$$\tilde{g}_i = \frac{1}{r} \log \left(\sum_{N^{(i)}} \exp \left(r \frac{\boldsymbol{\varphi}^{(i)}(\boldsymbol{\rho}) \circ (\Delta \mathbf{u}_i^{(i)} \cdot \mathbf{e}_z)}{d_w} \right) \right) - 1 + \boldsymbol{\kappa}^{(i)\top} \left(\mathbf{K}_{ff}^{(i)} \Delta \mathbf{u}_f^{(i)} - \mathbf{f}_f^{(i)} \right), \quad (\text{A.1})$$

where $\boldsymbol{\kappa}^{(i)}$ is a multiplier vector. The design derivative of \tilde{g}_i is:

$$\frac{\partial \tilde{g}_i}{\partial \boldsymbol{\rho}} = \frac{\partial (\Delta \mathbf{u}_f^{(i)})}{\partial \boldsymbol{\rho}} \mathbf{h}_i + \frac{\partial \boldsymbol{\varphi}^{(i)}}{\partial \boldsymbol{\rho}} \mathbf{q}_i + \boldsymbol{\kappa}^{(i)\top} \left(\frac{\partial \mathbf{K}_{ff}^{(i)}}{\partial \boldsymbol{\rho}} \Delta \mathbf{u}_f^{(i)} + \frac{\partial (\Delta \mathbf{u}_f^{(i)})}{\partial \boldsymbol{\rho}} \mathbf{K}_{ff}^{(i)} - \frac{\partial \mathbf{f}_f^{(i)}}{\partial \boldsymbol{\rho}} \right), \quad (\text{A.2})$$

with:

$$\mathbf{h}_i = \frac{1}{d_w \sum_{N^{(i)}} \exp \left(r \frac{\boldsymbol{\varphi}^{(i)}(\boldsymbol{\rho}) \circ (\Delta \mathbf{u}_i^{(i)} \cdot \mathbf{e}_z)}{d_w} \right)} \left(\exp \left(r \frac{\boldsymbol{\varphi}^{(i)}(\boldsymbol{\rho}) \circ (\Delta \mathbf{u}_i^{(i)} \cdot \mathbf{e}_z)}{d_w} \right) \circ \boldsymbol{\varphi}^{(i)}(\boldsymbol{\rho}) \right)$$

$$\mathbf{q}_i = \frac{1}{d_w \sum_{N^{(i)}} \exp \left(r \frac{\boldsymbol{\varphi}^{(i)}(\boldsymbol{\rho}) \circ (\Delta \mathbf{u}_i^{(i)} \cdot \mathbf{e}_z)}{d_w} \right)} \left(\exp \left(r \frac{\boldsymbol{\varphi}^{(i)}(\boldsymbol{\rho}) \circ (\Delta \mathbf{u}_i^{(i)} \cdot \mathbf{e}_z)}{d_w} \right) \circ (\Delta \mathbf{u}_i^{(i)} \cdot \mathbf{e}_z) \right)$$

After sorting the terms with $\partial (\Delta \mathbf{u}_f^{(i)}) / \partial \boldsymbol{\rho}$:

$$\frac{\partial \tilde{g}_i}{\partial \boldsymbol{\rho}} = \frac{\partial (\Delta \mathbf{u}_f^{(i)})}{\partial \boldsymbol{\rho}} \left(\mathbf{h}_i + \mathbf{K}_{ff}^{(i)\top} \boldsymbol{\kappa}^{(i)} \right) + \frac{\partial \boldsymbol{\varphi}^{(i)}}{\partial \boldsymbol{\rho}} \mathbf{q}_i + \boldsymbol{\kappa}^{(i)\top} \left(\frac{\partial \mathbf{K}_{ff}^{(i)}}{\partial \boldsymbol{\rho}} \Delta \mathbf{u}_f^{(i)} - \frac{\partial \mathbf{f}_f^{(i)}}{\partial \boldsymbol{\rho}} \right), \quad (\text{A.3})$$

$\boldsymbol{\kappa}_i$ is solved from:

$$\mathbf{K}_{ff}^{(i)\top} \boldsymbol{\kappa}^{(i)} = -\mathbf{h}_i \quad (\text{A.4})$$

and the sensitivity of g_i is calculated as:

$$\frac{\partial g_i}{\partial \boldsymbol{\rho}} = \frac{\partial \boldsymbol{\varphi}^{(i)}}{\partial \boldsymbol{\rho}} \mathbf{q}_i + \boldsymbol{\kappa}^{(i)\top} \left(\frac{\partial \mathbf{K}_{ff}^{(i)}}{\partial \boldsymbol{\rho}} \Delta \mathbf{u}_f^{(i)} - \frac{\partial \mathbf{f}_f^{(i)}}{\partial \boldsymbol{\rho}} \right). \quad (\text{A.5})$$

A.2. Sensitivity of the global distortion constraint

To obtain the sensitivity of the distortion constraint g_d , Eq. (18) is augmented by the equilibrium Eqs. (6) and (9) as well as the equation for evolution of the reaction forces (7):

$$\begin{aligned} \tilde{g}_d &= \frac{1}{2} \mathbf{d}^T \mathbf{d} - \frac{1}{2} d_{\max}^2 + \boldsymbol{\lambda}^{(M+1)T} \left(\mathbf{K}_{ff}^{(M+1)} \Delta \mathbf{u}_f^{(M+1)} + \mathbf{S}_f \mathbf{r}_0^{(M)} \right) \\ &+ \sum_{i=1}^M \boldsymbol{\lambda}^{(i)T} \left(\mathbf{K}_{ff}^{(i)} \Delta \mathbf{u}_f^{(i)} - \mathbf{f}_f^{(i)} \right) + \sum_{i=1}^M \boldsymbol{\mu}^{(i)T} \left(\mathbf{r}_0^{(i)} - \mathbf{r}_0^{(i-1)} - \mathbf{K}_{0f} \Delta \mathbf{u}_f^{(i)} \right), \end{aligned} \tag{A.6}$$

where $\boldsymbol{\lambda}$ and $\boldsymbol{\mu}$ are multiplier vectors and \mathbf{d} is defined in Eq. (17). The design derivative of \tilde{g}_d is:

$$\begin{aligned} \frac{\partial \tilde{g}_d}{\partial \boldsymbol{\rho}} &= \mathbf{d}^T \left(\sum_{i=j}^{M+1} \mathbf{Z}^{(i)} \frac{\partial (\Delta \mathbf{u}_f^{(i)})}{\partial \boldsymbol{\rho}} \right) \\ &+ \boldsymbol{\lambda}^{(M+1)T} \left(\frac{\partial \mathbf{K}_{ff}^{(M+1)}}{\partial \boldsymbol{\rho}} \Delta \mathbf{u}_f^{(M+1)} + \mathbf{K}_{ff}^{(M+1)} \frac{\partial (\Delta \mathbf{u}_f^{(M+1)})}{\partial \boldsymbol{\rho}} + \mathbf{S}_f \frac{\partial \mathbf{r}_0^{(M)}}{\partial \boldsymbol{\rho}} \right) \\ &+ \sum_{i=1}^M \boldsymbol{\lambda}^{(i)T} \left(\frac{\partial \mathbf{K}_{ff}^{(i)}}{\partial \boldsymbol{\rho}} \Delta \mathbf{u}_f^{(i)} + \mathbf{K}_{ff}^{(i)} \frac{\partial (\Delta \mathbf{u}_f^{(i)})}{\partial \boldsymbol{\rho}} - \frac{\partial \mathbf{f}_f^{(i)}}{\partial \boldsymbol{\rho}} \right) \\ &+ \sum_{i=1}^M \boldsymbol{\mu}^{(i)T} \left(\frac{\partial \mathbf{r}_0^{(i)}}{\partial \boldsymbol{\rho}} - \frac{\partial \mathbf{r}_0^{(i-1)}}{\partial \boldsymbol{\rho}} - \frac{\partial \mathbf{K}_{0f}^{(i)}}{\partial \boldsymbol{\rho}} \Delta \mathbf{u}_f^{(i)} - \mathbf{K}_{0f}^{(i)} \frac{\partial (\Delta \mathbf{u}_f^{(i)})}{\partial \boldsymbol{\rho}} \right). \end{aligned} \tag{A.7}$$

Next, the terms with $\partial(\Delta \mathbf{u})/\partial \boldsymbol{\rho}$ and $\partial \mathbf{r}/\partial \boldsymbol{\rho}$ are sorted per step, whereafter a series of equations is obtained for the multiplier vectors:

$$\mathbf{K}_{ff}^{(M+1)T} \boldsymbol{\lambda}^{(M+1)} = -\mathbf{Z}^{(M+1)T} \mathbf{d}, \tag{A.8}$$

$$\boldsymbol{\mu}^{(M)} = -\mathbf{S}_f^T \boldsymbol{\lambda}^{(M+1)}, \tag{A.9}$$

$$\boldsymbol{\mu}^{(i-1)} = \boldsymbol{\mu}^{(i)} \quad 1 \leq i \leq M, \tag{A.10}$$

$$\mathbf{K}_{ff}^{(i)T} \boldsymbol{\lambda}^{(i)} = \mathbf{K}_{f0}^{(i)} \boldsymbol{\mu}^{(i)} - \mathbf{Z}^{(i)T} \mathbf{d} \quad j \leq i \leq M, \tag{A.11a}$$

$$\mathbf{K}_{ff}^{(i)T} \boldsymbol{\lambda}^{(i)} = \mathbf{K}_{f0}^{(i)} \boldsymbol{\mu}^{(i)} \quad 1 \leq i \leq j-1, \tag{A.11b}$$

which are solved in reversed order of building steps [13,62,63]. Then the sensitivity of g_d is calculated as:

$$\begin{aligned} \frac{\partial g_d}{\partial \boldsymbol{\rho}} &= \boldsymbol{\lambda}^{(M+1)T} \left(\frac{\partial \mathbf{K}_{ff}^{(M+1)}}{\partial \boldsymbol{\rho}} \Delta \mathbf{u}_f^{(M+1)} \right) + \sum_{i=1}^M \boldsymbol{\lambda}^{(i)T} \left(\frac{\partial \mathbf{K}_{ff}^{(i)}}{\partial \boldsymbol{\rho}} \Delta \mathbf{u}_f^{(i)} - \frac{\partial \mathbf{f}_f^{(i)}}{\partial \boldsymbol{\rho}} \right) \\ &- \sum_{i=1}^M \boldsymbol{\mu}^{(i)T} \left(\frac{\partial \mathbf{K}_{0f}^{(i)}}{\partial \boldsymbol{\rho}} \Delta \mathbf{u}_f^{(i)} \right). \end{aligned} \tag{A.12}$$

The length of $\boldsymbol{\mu}$ equals the number of degrees of freedom, which are released to simulate release from the base plate. Inspection of Eqs. (A.10) and (A.11) suggests that the sensitivity $\partial g_d/\partial \boldsymbol{\rho}$ can be calculated without resorting to reversed order evaluation. This is true but involves handling of full matrices instead of vectors. Therefore reverse order evaluation has been implemented.

References

[1] I. Gibson, D.W. Rosen, B. Stucker, Additive Manufacturing Technologies, Vol. 17, Springer, 2014.
 [2] M. Cotteleer, J. Joyce, 3D Opportunity: Additive manufacturing paths to performance, innovation, and growth, Deloitte Rev. 14 (2014) 5–19.
 [3] J.P. Kruth, P. Mercelis, J. Van Vaerenbergh, L. Froyen, M. Rombouts, Binding mechanisms in selective laser sintering and selective laser melting, Rapid Prototyp. J. (2005).

- [4] D. Gu, Laser Additive Manufacturing of High-Performance Materials, Springer, 2015.
- [5] L. Van Belle, G. Vansteenkiste, J.C. Boyer, Investigation of residual stresses induced during the selective laser melting process, in: Key Eng. Mater., 554, Trans Tech Publ, 2013, pp. 1828–1834.
- [6] J.P. Kruth, L. Froyen, J. Van Vaerenbergh, P. Mercelis, M. Rombouts, B. Lauwers, Selective laser melting of iron-based powder, J. Mater Process. Technol. 149 (1–3) (2004) 616–622.
- [7] A. Hussein, L. Hao, C.Z. Yan, R. Everson, Finite element simulation of the temperature and stress fields in single layers built without-support in selective laser melting, Mater. Des. 52 (52) (2013) 638–647.
- [8] J.C. Heigel, P. Michaleris, E.W. Reutzel, Thermo-mechanical model development and validation of directed energy deposition additive manufacturing of Ti–6Al–4V, Addit. Manuf. 5 (2015) 9–19.
- [9] W.E. Frazier, Metal additive manufacturing: a review, J. Mater. Eng. Perform. 23 (6) (2014) 1917–1928.
- [10] R.J. Silva, G.F. Barbosa, J. Carvalho, Additive manufacturing of metal parts by welding, IFAC-PapersOnLine 48 (3) (2015) 2318–2322.
- [11] J. Goldak, A. Chakravarti, M. Bibby, A new finite element model for welding heat sources, Metall. Trans. B 15 (2) (1984) 299–305.
- [12] P. Michaleris, Modeling metal deposition in heat transfer analyses of additive manufacturing processes, Finite Elem. Anal. Des. 86 (86) (2014) 51–60.
- [13] G. Allaire, L. Jakabčič, Taking into account thermal residual stresses in topology optimization of structures built by additive manufacturing, Math. Models Methods Appl. Sci. 28 (12) (2018) 2313–2366.
- [14] D. Deng, H. Murakawa, W. Liang, Numerical simulation of welding distortion in large structures, Comput. Methods Appl. Mech. Engrg. 196 (45–48) (2007) 4613–4627.
- [15] P. Michaleris, A. DeBiccardi, Prediction of welding distortion, Weld. J.-Incl. Weld. Res. Suppl. 76 (4) (1997) 172s.
- [16] P.-L. Mollicone, D. Camilleri, T.G.F. Gray, T. Comlekci, Simple thermo-elastic–plastic models for welding distortion simulation, J. Mater Process. Technol. 176 (1–3) (2006) 77–86.
- [17] N.S. Prasad, T.K.S. Narayanan, Finite element analysis of temperature distribution during arc welding using adaptive grid technique, Weld. J. (Miami, Fla) 75 (4) (1996) 123s–128s.
- [18] H. Runnemalm, S. Hyun, Three-dimensional welding analysis using an adaptive mesh scheme, Comput. Methods Appl. Mech. Engrg. 189 (2) (2000) 515–523.
- [19] X.K. Zhu, Y.J. Chao, Effects of temperature-dependent material properties on welding simulation, Comput. Struct. 80 (11) (2002) 967–976.
- [20] E.R. Denlinger, M. Gouge, J. Irwin, P. Michaleris, Thermomechanical model development and in situ experimental validation of the laser powder-bed fusion process, Addit. Manuf. 16 (2017) 73–80.
- [21] R.K. Chin, J.L. Beuth, C.H. Amon, Thermomechanical modeling of successive material deposition in layered manufacturing, in: Solid Freeform Fabrication Proceedings. Proc. 1996 Solid Freeform Fabrication Symposium, Austin, 1996.
- [22] N.W. Klingbeil, J.L. Beuth, R.K. Chin, C.H. Amon, Measurement and modeling of residual stress-induced warping in direct metal deposition processes, in: Solid Freeform Fabrication Proceedings. Proc. 1998 Solid Freeform Fabrication Symposium, Austin, 1998, pp. 367–374.
- [23] M. Matsumoto, M. Shiomi, K. Osakada, F. Abe, Finite element analysis of single layer forming on metallic powder bed in rapid prototyping by selective laser processing, Int. J. Mach. Tools Manuf. 42 (1) (2002) 61–67.
- [24] A.H. Nickel, D.M. Barnett, F.B. Prinz, Thermal stresses and deposition patterns in layered manufacturing, Mater. Sci. Eng. A-Struct. Mater. Prop. Microstruct. Process. 317 (1–2) (2001) 59–64.
- [25] K. Dai, L. Shaw, Distortion minimization of laser-processed components through control of laser scanning patterns, Rapid Prototyp. J. 8 (5) (2002) 270–276.
- [26] N.E. Hodge, R.M. Ferencz, J.M. Solberg, Implementation of a thermomechanical model for the simulation of selective laser melting, Comput. Mech. 54 (1) (2014) 33–51.
- [27] M. Nikoukar, N. Patil, D. Pal, B.E. Stucker, Methods for enhancing the speed of numerical calculations for the prediction of the mechanical behavior of parts made using additive manufacturing, in: Solid Freeform Fabrication Proceedings. Proc. 2013 Solid Freeform Fabrication Symposium, Austin, 2013.
- [28] N. Patil, D. Pal, R.H. Khalid, K. Zeng, A. Moreland, A. Hicks, D. Beeler, B.E. Stucker, A generalized feed forward dynamic adaptive mesh refinement and derefinement finite element framework for metal laser sintering - Part I: Formulation and algorithm development, J. Manuf. Sci. Eng. 137 (4) (2015) 041001.
- [29] K. Zeng, D. Pal, N. Patil, B.E. Stucker, A new dynamic mesh method applied to the simulation of selective laser melting, in: Proceedings of the Solid Freeform Fabrication Symposium, Austin, TX, August 2013, 2013, pp. 12–14.
- [30] C. Li, C.H. Fu, Y.B. Guo, F.Z. Fang, A multiscale modeling approach for fast prediction of part distortion in selective laser melting, J. Mater Process. Technol. 229 (2016) 703–712.
- [31] N. Keller, V. Ploshikhin, New method for fast predictions of residual stress and distortion of AM parts, in: Solid Freeform Fabrication, 2014.
- [32] F. Neugebauer, N. Keller, V. Ploshikhin, F. Feuerhahn, H. Köhler, Multi scale FEM simulation for distortion calculation in additive manufacturing of hardening stainless steel, in: Proc. Int. Workshop on ‘Thermal Forming and Welding Distortion’, 2014.
- [33] J. Schilp, C. Seidel, H. Krauss, J. Weirather, Investigations on temperature fields during laser beam melting by means of process monitoring and multiscale process modelling, Adv. Mech. Eng. 6 (2014).
- [34] P. Alvarez, J. Ecenarro, I. Setien, M.S. Sebastian, A. Echeverria, L. Eciolaza, Computationally efficient distortion prediction in powder bed fusion additive manufacturing, Int. J. Eng. Res. Sci. 2 (10) (2016) 39–46.
- [35] T.A. Krol, S. Westhäuser, M.F. Zäh, J. Schilp, C. Groth, Development of a simulation-based process chain-strategy for different levels of detail for the preprocessing definitions, SNE Simul. Notes Europe 21 (2011) 135–140.

- [36] C. Seidel, M.F. Zäh, M. Wunderer, J. Weirather, T.A. Krol, M. Ott, Simulation of the laser beam melting process – approaches for an efficient modelling of the beam-material interaction, *Proc. CIRP* 25 (2014) 146–153.
- [37] M.F. Zäh, G. Branner, Investigations on residual stresses and deformations in selective laser melting, *Prod. Eng.* 4 (1) (2009) 35–45.
- [38] V.D. Savane, R. Fu, P. Gaborik, C. Chin, Distortion prediction of Ti6Al4V parts in selective laser melting: An industrial case study, in: *AIAA Scitech 2020 Forum*, 2020, p. 1475.
- [39] M. Seabra, J. Azevedo, A. Araújo, L. Reis, E. Pinto, N. Alves, R. Santos, J.P. Mortágua, Selective laser melting (SLM) and topology optimization for lighter aerospace components, *Proc. Struct. Integr.* 1 (2016) 289–296.
- [40] M.P. Bendsøe, O. Sigmund, *Topology Optimization. Theory, Methods, and Applications*, Springer Verlag, New York, 2003.
- [41] J. Liu, A.T. Gaynor, S. Chen, Z. Kang, K. Suresh, A. Takezawa, L. Li, J. Kato, J. Tang, C.C.L. Wang, L. Cheng, X. Liang, A.C. To, Current and future trends in topology optimization for additive manufacturing, *Struct. Multidiscip. Optim.* 57 (6) (2018) 2457–2483.
- [42] S. Afazov, W. Denmark, B.L. Toralles, A. Holloway, A. Yaghi, Distortion prediction and compensation in selective laser melting, *Addit. Manuf.* 17 (2017) 15–22.
- [43] R.A. Wildman, A.T. Gaynor, *Topology Optimization for Reducing Additive Manufacturing Processing Distortions*, Report ARL-TR-8242, Weapons and Materials Research Directorate, US Army Research Laboratory, Aberdeen Proving Ground, United States, 2017.
- [44] A. Takezawa, A.C. To, Q. Chen, X. Liang, F. Dugast, X. Zhang, M. Kitamura, Sensitivity analysis and lattice density optimization for sequential inherent strain method used in additive manufacturing process, *Comput. Methods Appl. Mech. Engrg.* 370 (2020) 113–231.
- [45] K. Bartsch, F. Lange, M. Gralow, C. Emmelmann, Novel approach to optimized support structures in laser beam melting by combining process simulation with topology optimization, *J. Laser Appl.* 31 (2) (2019) 022302.
- [46] L. Cheng, X. Liang, J. Bai, Q. Chen, J. Lemon, A. To, On utilizing topology optimization to design support structure to prevent residual stress induced build failure in laser powder bed metal additive manufacturing, *Addit. Manuf.* 27 (2019) 290–304.
- [47] J. Pellens, G. Lombaert, M. Michiels, T. Craeghs, M. Schevenels, Topology optimization of support structure layout in metal-based additive manufacturing accounting for thermal deformations, *Struct. Multidiscip. Optim.* 61 (6) (2020) 2291–2303.
- [48] Z.-D. Zhang, O. Ibhadode, U. Ali, C.F. Dibia, P. Rahnema, A. Bonakdar, E. Toyserkani, Topology optimization parallel-computing framework based on the inherent strain method for support structure design in laser powder-bed fusion additive manufacturing, *Int. J. Mech. Mater. Des.* (2020).
- [49] Y. Ueda, M.G. Yuan, Prediction of residual stresses in butt welded plates using inherent strains, *J. Eng. Mater. Technol.* 115 (4) (1993) 417–423.
- [50] Q. Chen, X. Liang, D. Hayduke, J. Liu, L. Cheng, J. Oskin, R. Whitmore, A.C. To, An inherent strain based multiscale modeling framework for simulating part-scale residual deformation for direct metal laser sintering, *Addit. Manuf.* 28 (2019) 406–418.
- [51] I. Setien, M. Chiumenti, S. van der Veen, M. San Sebastian, F. Garcíandía, A. Echeverría, Empirical methodology to determine inherent strains in additive manufacturing, *Comput. Math. Appl.* 78 (2018) 2282–2295.
- [52] D. Munro, C. Ayas, M. Langelaar, A. Van Keulen, On process-step parallel computability and linear superposition of mechanical responses in additive manufacturing process simulation, *Addit. Manuf.* 28 (2019) 738–749.
- [53] M.P. Bendsøe, Optimal shape design as a material distribution problem, *Struct. Optim.* 1 (4) (1989) 193–202.
- [54] O. Sigmund, Morphology-based black and white filters for topology optimization, *Struct. Multidiscip. Optim.* 33 (4–5) (2007) 401–424.
- [55] G. Kreisselmeier, R. Steinhauser, Systematic control design by optimizing a vector performance index, in: *IFAC Symposium on Computer-Aided Design of Control Systems*, Zurich, 1979.
- [56] J.L. Lions, *Optimal Control of Systems Governed by Partial Differential Equations*, in: *Grundlehren der Mathematischen Wissenschaften*, vol. 170, Springer, 1971.
- [57] K. Svanberg, The method of moving asymptotes - a new method for structural optimization, *Internat. J. Numer. Methods Engrg.* 24 (2) (1987) 359–373.
- [58] X. Liang, L. Cheng, Q. Chen, Q. Yang, A.C. To, A modified method for estimating inherent strains from detailed process simulation for fast residual distortion prediction of single-walled structures fabricated by directed energy deposition, *Addit. Manuf.* 23 (2018) 471–486.
- [59] M. Siewert, F. Neugebauer, J. Epp, V. Ploshikhin, Validation of mechanical layer equivalent method for simulation of residual stresses in additive manufactured components, *Comput. Math. Appl.* 78 (7) (2019) 2407–2416.
- [60] G.M. Ter Haar, T.H. Becker, Selective laser melting produced Ti-6Al-4V: Post-process heat treatments to achieve superior tensile properties, *Materials* 11 (1) (2018) 146.
- [61] Y. Luo, O. Sigmund, Q. Li, S. Liu, Additive manufacturing oriented topology optimization of structures with self-supported enclosed voids, *Comput. Methods Appl. Mech. Engrg.* 372 (2020) 113385.
- [62] P. Michaleris, D. Tortorelli, C.A. Vidal, Tangent operators and design sensitivity formulations for transient non-linear coupled problems with applications to elastoplasticity, *Internat. J. Numer. Methods Engrg.* 37 (1994) 2471–2499.
- [63] S.H. Chung, L. Fourment, J.L. Chenot, S.M. Hwang, Adjoint state method for shape sensitivity analysis in non-steady forming applications, *Internat. J. Numer. Methods Engrg.* 57 (2003) 1431–1444.